Electronic excitations investigated by inelastic x-ray scattering spectroscopy

2001 J. Phys.: Condens. Matter 13 7557

(http://iopscience.iop.org/0953-8984/13/34/307)

INSTITUTE OF PHYSICS PUBLISHING JOURNAL OF PHYSICS: CONDENSED MATTER

J. Phys.: Condens. Matter **13** (2001) 7557–7591 PII: S0953-8984(01)24031-4

Electronic excitations investigated by inelastic x-ray scattering spectroscopy

W Schülke

Institute of Physics, University of Dortmund, D-44221 Dortmund, Germany

E-mail: schuelke@physik.uni-dortmund.de

Received 18 April 2001
Published 9 August 2001
Online at stacks.iop.org/JPhysCM/13/7557

Abstract

It is shown how non-resonant and resonant inelastic x-ray scattering spectroscopy (IXSS) offer valuable information about electronic excitations in solids. After a presentation of the basic relations, applications of IXSS on a large variety of systems and electronic excitations are discussed, where in most cases synchrotron radiation is utilized

1. Introduction

It was first pointed out by Nozieres and Pines [1] that the spectral analysis of inelastically scattered x-rays can give valuable information about the frequency and wavevector-dependent response function as defined by electronic excitations of the scattering system. Decisive for developing this x-ray technique was the advantage of inelastic x-ray scattering spectroscopy (IXSS) over electron energy loss spectroscopy (EELS) which is due to a much smaller contribution of multiple scattering of the former, especially for larger momentum transfer. First experiments on simple low-Z metals, still performed with conventional x-ray sources, were mainly devoted to the measurement of the dispersion of the plasmon loss [2–4] or to the demonstration of the role of Coulomb correlation in the response function [5]. However, there also came up studies of the dynamic structure factor $S(\boldsymbol{q}, \omega)$ in the region of intermediate momentum transfer $\boldsymbol{q}$ [6–10]. The detection of a two-peak or multi-peak fine structure of $S(\boldsymbol{q}, \omega)$ and its interpretation by Platzman and Eisenberger [6] as an indication of an incipient Wigner electron lattice prompted much theoretical work on the dynamic structure of electrons in nearly homogeneous systems, the state of which in the mid 1980s was reviewed in [11], at the time when synchrotron radiation was used for the first time for measurements of the dynamic structure factor of simple metals [12]. Already a while before, however, Eisenberger *et al* [13, 14] utilized for the first time synchrotron radiation in a resonant inelastic x-ray scattering experiment, where the shift of an x-ray emission line was observed, which occurs when the excitation energy approaches the core excitation threshold (today designated by Raman shift).

0953-8984/01/347557+35$30.00

In what follows, a review of all aspects of IXSS with synchrotron radiation is presented as far as the investigation of electronic excitations is concerned. (Therefore, the so-called Compton regime of inelastic x-ray scattering is excepted, since, within the limits of the impulse approximation, this regime provides information about ground-state properties of the scattering electron system rather than about excitations.)

In section 2 non-resonant IXSS is reviewed starting with some basic relations (subsection 2.1) followed by several aspects of the dynamic structure factor of electrons in simple metals and s–p-bonded semiconductors: plasmons and the transition to the particle–hole continuum (subsection 2.2); band structure effects of IXS spectra (subsection 2.3); core excitation in IXSS (subsection 2.4); interpretation of IXS spectra going beyond the random phase approximation (subsection 2.5).

Section 3 is devoted to a particular variant of non-resonant inelastic x-ray scattering, where the initial photon state is a wave field consisting of two coherently superimposed plane waves. We call this variant coherent inelastic x-ray scattering spectroscopy (CIXSS). Subsection 3.1 introduces the basics, especially the peculiarities of off-diagonal response, which can be investigated by means of CIXSS. Subsection 3.2 shows how the information about off-diagonal response can be obtained experimentally, and subsection 3.3 deals with the investigation of the plasmon band structure by means of CIXSS; subsection 3.4 shows how the superposition of excitations into the quasi-particle continuum with excitation of Umklapp-plasmon bands give rise to so-called plasmon Fano resonances seen in the IXS spectra of Si and Li.

Finally section 4 presents a review of resonant inelastic x-ray scattering spectroscopy (RIXSS). After some basics in subsection 4.1, applications to investigations of electronic excitations are shown. In subsection 4.2 some applications of core-level RIXS spectra are demonstrated. The next subsections 4.3 and 4.4 show how the coherence between the absorption and re-emission processes via the intermediate state in RIXSS and the corresponding conservation rules of momentum and spin lead to Bloch-$\boldsymbol{k}$- and spin-selective spectroscopies, respectively. A special subsection 4.5 presents most recent results, where shakeup processes in the intermediate state of RIXSS can present valuable information about electronic excitation processes in new materials, which are otherwise hardly obtainable.

2. Non-resonant inelastic x-ray scattering

2.1. Basic relations

Neglecting contributions of off-diagonal response (see subsection 3.1) the double differential scattering cross section (DDCS) of non-resonant IXSS is given by [15]

$$\mathrm{d}^2\sigma/\mathrm{d}\Omega\,\mathrm{d}\omega = (\mathrm{d}\sigma/\mathrm{d}\Omega)_{Th}S(\boldsymbol{q},\omega) \tag{2.1}$$

where $(\mathrm{d}\sigma/\mathrm{d}\Omega)_{Th}$ is the Thomson cross section and $S(\boldsymbol{q},\omega)$ the dynamic structure factor, which contains the information about electronic excitations via the imaginary part of the dielectric response function $1/\varepsilon(\boldsymbol{q},\omega)$:

$$S(\boldsymbol{q},\omega) = (-\hbar q^2/4\pi^2e^2n)\mathrm{Im}\,[1/\varepsilon(\boldsymbol{q},\omega)] \tag{2.2}$$

where $\boldsymbol{q}$ is the momentum and $\hbar\omega$ the energy transferred to the scattering system in the inelastic scattering process, and n the electron density of the scattering system. The dielectric response function is directly related to the polarization function $\chi(\boldsymbol{q},\omega)$

$$1/\varepsilon(\boldsymbol{q},\omega) = 1 + v(\boldsymbol{q})\chi(\boldsymbol{q},\omega) \qquad v(\boldsymbol{q}) = 4\pi e^2/q^2 \tag{2.3}$$

where $\chi(\boldsymbol{q},\omega)$ connects the Fourier transformed induced charge $n_{ind}(\boldsymbol{q},\omega)$ with the Fourier transform of the external potential $\phi_{ext}(\boldsymbol{q},\omega)$:

$$n_{ind}(\boldsymbol{q},\omega) = -e\chi(\boldsymbol{q},\omega)\phi_{ext}(\boldsymbol{q},\omega). \tag{2.4}$$

The basic ingredient of the polarization function is the so-called Lindhard [16] polarization function $\chi_0(\boldsymbol{q},\omega)$, which describes the polarization of an homogeneous electron system by taking into account all single-particle excitation processes (particle–hole excitations) mediated by the momentum transfer $\boldsymbol{q}$, assuming they are allowed by Pauli's principle, but neglecting both the interaction of the particle and the hole with the surrounding electron fluid as well as any interaction between the particle and the hole left behind, so that $\chi_0(\boldsymbol{q},\omega)$ reads

$$\chi_0(\boldsymbol{q},\omega) = 2\lim_{\eta\to+0}\sum_{\boldsymbol{k}}[f(\varepsilon_{\boldsymbol{k}}) - f(\varepsilon_{\boldsymbol{k}+\boldsymbol{q}})]/(\hbar\omega + \varepsilon_{\boldsymbol{k}} - \varepsilon_{\boldsymbol{k}+\boldsymbol{q}} + \mathrm{i}\eta) \tag{2.5}$$

where $f(\varepsilon_{\boldsymbol{k}})$ is the Fermi function and $\varepsilon_{\boldsymbol{k}}$ is the free electron kinetic energy $\hbar^2k^2/2m$. Equation (2.5) can also be written in terms of 'undressed' one-particle Green's functions:

$$\chi_0(\boldsymbol{q},\omega) = 2\int(\mathrm{d}\varepsilon/2\pi\mathrm{i})\int(\mathrm{d}^3k/8\pi^3)G^0(\boldsymbol{k},\varepsilon)G^0(\boldsymbol{k}+\boldsymbol{q},\varepsilon+\omega) \tag{2.6}$$

so that $\chi_0(\boldsymbol{q},\omega)$ can be represented by the very instructive and compact diagram of figure 1. The 'undressed' Green's function $G^0(\boldsymbol{k},\varepsilon)$ is given by

$$G^0(\boldsymbol{k},\varepsilon) = \Theta^<(\boldsymbol{k})/(\varepsilon - \varepsilon_{\boldsymbol{k}} - \mathrm{i}\eta) + \Theta^>(\boldsymbol{k})/(\varepsilon - \varepsilon_{\boldsymbol{k}} + \mathrm{i}\eta) \qquad \eta\to+0 \tag{2.7}$$

$$\Theta^<(\boldsymbol{k})\begin{cases}1 & \text{for } k \leqslant k_F\\ 0 & \text{for } k > k_F\end{cases} \qquad k_F = \text{ Fermi momentum} \tag{2.8}$$

$$\Theta^>(\boldsymbol{k}) = 1 - \Theta^<(\boldsymbol{k}).$$

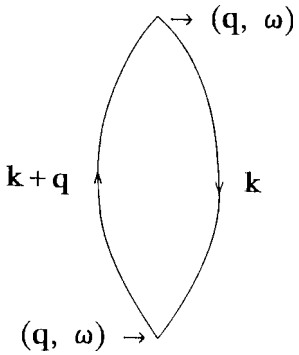

Figure 1. Diagram representing the Lindhard polarization function. The propagators are 'undressed' one-particle Green's functions.

A first step of approximating the polarization function in terms of the Lindhard $\chi_0(\boldsymbol{q},\omega)$ is the so-called random phase approximation (RPA), where in (2.4) $\chi(\boldsymbol{q},\omega)$ is replaced by $\chi_0(\boldsymbol{q},\omega)$ and $\phi_{ext}(\boldsymbol{q},\omega)$ is replaced by $\phi_{ext}(\boldsymbol{q},\omega) + v(\boldsymbol{q})n_{ind}(\boldsymbol{q},\omega)$, so that, additionally to the external potential $\phi_{ext}(\boldsymbol{q},\omega)$, the potential due to the induced polarization also acts on the system:

$$n_{ind}(\boldsymbol{q},\omega) = -e\chi_0(\boldsymbol{q},\omega)[\phi_{ext}(\boldsymbol{q},\omega) + v(\boldsymbol{q})n_{ind}(\boldsymbol{q},\omega)] \tag{2.9}$$

$$n_{ind}(\boldsymbol{q},\omega) = -e\{\chi_0(\boldsymbol{q},\omega)[1 - v(\boldsymbol{q})\chi_0(\boldsymbol{q},\omega)]\}\phi_{ext}(\boldsymbol{q},\omega) \tag{2.10}$$

$$\chi_{RPA}(\boldsymbol{q},\omega) = \chi_0(\boldsymbol{q},\omega)/[1 - v(\boldsymbol{q})\chi_0(\boldsymbol{q},\omega)] \tag{2.11}$$

and according to (2.3)

$$1/\varepsilon_{RPA}(\boldsymbol{q},\omega) = 1 + v(\boldsymbol{q})\chi_{RPA}(\boldsymbol{q},\omega) \tag{2.12}$$

and by inserting (2.11)

$$\varepsilon_{RPA}(\boldsymbol{q},\omega) = 1 - v(\boldsymbol{q})\chi_0(\boldsymbol{q},\omega) \tag{2.13}$$

so that the dynamic structure factor within the limits of the RPA, $S_{RPA}(\boldsymbol{q},\omega)$, is determined by

$$\begin{aligned} S_{RPA}(\boldsymbol{q},\omega) &= (-\hbar q^2/4\pi^2 e^2 n)\mathrm{Im}\,[1/\varepsilon_{RPA}(\boldsymbol{q},\omega)] \\ &= (\hbar q^2/4\pi^2 e^2 n)\mathrm{Im}\,[\varepsilon_{RPA}(\boldsymbol{q},\omega)]/|\varepsilon_{RPA}(\boldsymbol{q},\omega)|^2. \end{aligned} \tag{2.14}$$

In what follows this relation and further improvements of the RPA will be used to understand the dynamic structure of simple metals and s–p-bound semiconductors as obtained by synchrotron radiation based measurements.

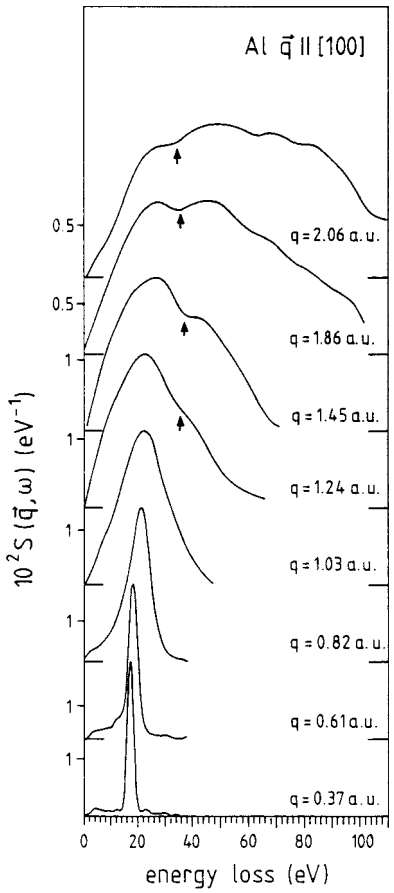

Figure 2. Measured dynamic structure factor $S(\boldsymbol{q},\omega)$ of Al metal for $\boldsymbol{q} \parallel [100]$ and different values of q as indicated.

2.2. Plasmons and transition to the particle–hole continuum

Figure 2 shows the structure factor $S(\boldsymbol{q},\omega)$ of Al for $\boldsymbol{q} \parallel [100]$ for different values of q as obtained with monochromatized synchrotron radiation (7.99 keV) from the DORIS storage

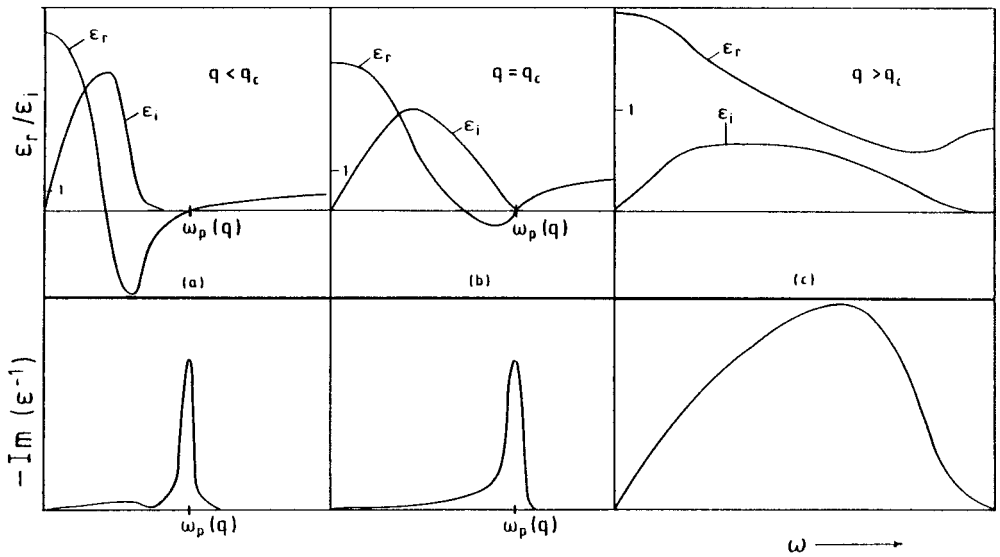

Figure 3. Upper panel: Real (ε_r) and imaginary (ε_i) part of the RPA dielectric function $\varepsilon_{RPA}(\boldsymbol{q}, \omega)$ for $q < q_c$, $q = q_c$ and $q > q_c$. Lower panel: Corresponding imaginary part of $-\varepsilon^{-1}_{RPA}(\boldsymbol{q}, \omega)$.

ring using energy analysis of scattered radiation in inverse geometry, overall energy resolution 1.6 eV [17]. The transition from a very sharp structure for $q < 0.8$ a.u. (a.u. = atomic units: $\hbar = e = m = 1$) to a much broader one can be understood as a transition from plasmon excitation to excitation into the particle–hole continuum by looking at figure 3, where for three different values of q the real and imaginary parts of $\varepsilon_{RPA}(\boldsymbol{q}, \omega)$ are shown, together with the corresponding $-\mathrm{Im}\,[1/\varepsilon_{RPA}(\boldsymbol{q}, \omega)] \sim S(\boldsymbol{q}, \omega)$. A sharp structure of $S(\boldsymbol{q}, \omega)$ originates at that frequency ω_p (plasma frequency), where $\mathrm{Re}\,[\varepsilon_{RPA}(\boldsymbol{q}, \omega)]$ has a zero passage and where simultaneously also $\mathrm{Im}\,[\varepsilon_{RPA}(\boldsymbol{q}, \omega)]$ is nearly equal to zero, both necessary conditions for the plasma oscillation of the electron system to be a good (nearly undamped) elementary excitation [18]. This behaviour exists up to the so-called critical momentum transfer q_c, where the zero passage of $\mathrm{Re}\,[\varepsilon_{RPA}(\boldsymbol{q}, \omega)]$ just coincides with the high-ω edge of $\mathrm{Im}\,[\varepsilon_{RPA}(\boldsymbol{q}, \omega)]$. Within the region $q < q_c$, the q-dependence of the $S(\boldsymbol{q}, \omega)$ peak position can be utilized to meausre the plasmon dispersion $\omega_p(\boldsymbol{q})$, as done with IXSS for Li [3, 11, 19] and Be [4], although those investigations are the domain of EELS [20], since the differential cross section for electron scattering goes like q^{-2}. For $q > q_c$ the plasmons can decay into particle–hole excitations. Thus they become strongly damped. Now particle–hole excitations, which cover a broad ω-continuum, dominate the dynamic structure factor. The same behaviour has been found for Li [3, 11, 19], Be [4, 21] and Na [19].

It is a unique domain of IXSS to investigate the plasmon dispersion of liquid metals, as has been done by Hills *et al* [19] for Li and Na and by Sternemann *et al* for Al [22]. Both papers come to the conclusion that the plasmon dispersion exhibits a jump at the melting temperature, which can simply be explained by expansion upon melting and the consequent reduction in density. But, more importantly, the deviation of the plasmon dispersion from the RPA prediction for a homogeneous electron gas, which is attributed to interband transitions [23], does not change upon melting. Therefore, it must be concluded that the short-range ionic correlations of a liquid are sufficient to produce a packing comparable with that of a solid, at least on a length scale probed by a plasmon.

2.3. Band structure effects of $S(\boldsymbol{q}, \omega)$

2.3.1. Excitation gap induced fine structure. The relation (2.5) for the Lindhard polarization function $\chi_0(\boldsymbol{q}, \omega)$ can be modified such that band structure effects are also admitted. The summation over $\boldsymbol{k}$ in (2.5) has to be replaced by a summation over the reduced Bloch wavevectors $\boldsymbol{k}$ and over the bands with index ν. Whereas in (2.5) the momentum transfer $\boldsymbol{q}$ allows only transitions from a free electron state with momentum $\boldsymbol{k}$ into a state with momentum $\boldsymbol{k} + \boldsymbol{q}$, now the probability for a transition from a Bloch state $|\boldsymbol{k}, \nu\rangle$ into another state $|\boldsymbol{k}', \nu'\rangle$ is regulated by the square of the matrix element $\langle \boldsymbol{k}', \nu' | \exp(\mathrm{i}\boldsymbol{q} \cdot \boldsymbol{r}) | \boldsymbol{k}\nu \rangle$, so that interband transitions also come into play. Therefore, one has to sum additionally over $\boldsymbol{k}'$ and ν', thus ending up with the well known Ehrenreich–Cohen [24] self-consistent field expression for the polarization function, $\chi_{sc}(\boldsymbol{q}, \omega)$, which is equivalent to the Lindhard expression $\chi_0(\boldsymbol{q}, \omega)$ and can replace it in the expression (2.11) for the RPA polarization function:

$$\chi_{sc}(\boldsymbol{q}, \omega) = \sum_{\substack{\boldsymbol{k},\nu \\ \boldsymbol{k}',\nu'}} |\langle \boldsymbol{k}'\nu' | \exp(\mathrm{i}\boldsymbol{q} \cdot \boldsymbol{r}) | \boldsymbol{k}\nu \rangle|^2 [f(\boldsymbol{k}', \nu') - f(\boldsymbol{k}, \nu)] \\ / [\hbar\omega + E(\boldsymbol{k}, \nu) - E(\boldsymbol{k}', \nu') + \mathrm{i}\eta] \tag{2.15}$$

where $E(\boldsymbol{k}, \nu)$ is the energy and $f(\boldsymbol{k}, \nu)$ the occupation number of the one-electron Bloch state $|\boldsymbol{k}, \nu\rangle$. The imaginary part of $\chi_{sc}(\boldsymbol{q}, \omega)$

$$\mathrm{Im}\, \chi_{sc}(\boldsymbol{q}, \omega) = \pi \sum_{\substack{\boldsymbol{k},\nu \\ \boldsymbol{k}',\nu'}} |\langle \boldsymbol{k}'\nu' | \exp(\mathrm{i}\boldsymbol{q} \cdot \boldsymbol{r}) | \boldsymbol{k}\nu \rangle|^2 [f(\boldsymbol{k}, \nu) \\ - f(\boldsymbol{k}', \nu')] \delta[\hbar\omega + E(\boldsymbol{k}, \nu) - E(\boldsymbol{k}', \nu')] \tag{2.16}$$

is then directly related to the combined density of occupied and unoccupied states via the energy conserving δ-function: $\delta[\hbar\omega + E(\boldsymbol{k}, \nu) - E(\boldsymbol{k}', \nu')]$.

The most prominent structure of $S(\boldsymbol{q}, \omega)$, at least for simple metals and s–p-bounded semiconductors, which arises by ion–electron interaction in crystalline solids, can be traced back to excitation gaps for final states on Bragg planes [25] in the extended zone scheme, perpendicular to $\boldsymbol{q}$. Within the limits of the so-called empty lattice model (neglecting the periodic lattice potential), final states on the Bragg planes belonging to different bands ν and ν' are degenerate and contribute to the same energy transfer ω. When the periodic potential is switched on, this degeneracy may be removed, so that an energy gap is opened, which leads to a corresponding excitation gap in the combined density of states. According to (2.15), this excitation gap is also present in $\mathrm{Im}\, \chi_{sc}(\boldsymbol{q}, \omega)$ and consequently in $\varepsilon_i \equiv \mathrm{Im}\, \varepsilon_{RPA}(\boldsymbol{q}, \omega)$, although this gap can be filled to a certain extent by other transitions. As shown in figure 4, a gap in ε_i can produce, via the Kramers–Kronig relation, an additional zero of $\varepsilon_r \equiv \mathrm{Re}\, \varepsilon_{RPA}(\boldsymbol{q}, \omega)$ or at least a strong minimum, which should give rise to a strong peak in $-\mathrm{Im}\,[1/\varepsilon_{RPA}(\boldsymbol{q}, \omega)]$ according to (2.14). Such a peak, if due to an additional zero of ε_i, can be interpreted as a new collective mode, the so-called zone-boundary collective state (ZBCS), first introduced by Foo and Hopfield [26] and thoroughly discussed by Sturm and Oliveira [27] for Al. Even if there is no strong peak in $-\mathrm{Im}\,[1/\varepsilon_{RPA}(\boldsymbol{q}, \omega)]$ due to a zero or nearly zero of ε_r, the excitation gap is prominent by its dip in ε_i.

Excitation gap induced fine structure of $S(\boldsymbol{q}, \omega)$ for $q > q_c$ was first found in IXS spectra of Li by Schülke *et al* [11] and discussed on the basis of a pseudopotential band structure calculation of $S(\boldsymbol{q}, \omega)$. The peak structure of $S(\boldsymbol{q}, \omega)$ around 10 eV, as shown in figure 5, can be directly traced back to an excitation gap opened by the potential coefficient V_{200} for final states on the $\boldsymbol{g}_{200}$–Bragg plane. A ZBCS-like peak structure due to the $\boldsymbol{g}_{110}$–Bragg plane of Li and its dispersion was also investigated by Schülke *et al* and with 40 meV resolution by the Burkel group [28]. A peak–dip or dip structure in $S(\boldsymbol{q}, \omega)$ was found in an IXSS experiment

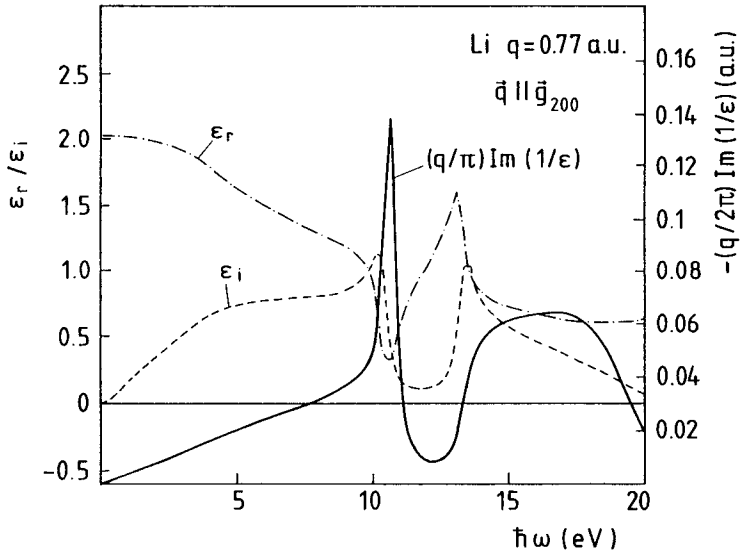

Figure 4. Quasi-excitation gap in the imaginary part ε_i of the RPA dielectric function of Li: $\boldsymbol{q} \| \boldsymbol{g}_{200}$, $q = 0.77$ a.u., according to a local empirical pseudopotential calculation, together with the corresponding real part ε_r and the loss function $-\mathrm{Im}\,[\varepsilon^{-1}(\boldsymbol{q}, \omega)]$.

also for Be [21, 29] and was interpreted by pseudopotential calculations as being induced by band structure related excitation gaps. As shown in [29] by means of Kramers–Kronig analysis of the experimental data, the $\boldsymbol{q} \parallel [100]$ spectra of Be for $q = 0.77$ a.u. exhibit a very pronounced peak, which can be attributed to a zero-passage of ε_r for $q > q_c$, and must therefore be considered as a pure ZBCS. The interpretation of the $S(\boldsymbol{q}, \omega)$ fine structure of Be on the basis of Bragg-plane induced excitation gaps in [21, 29] found full confirmation by *ab initio* band structure calculations of the dynamic response of Be performed by Maddocks *et al* [30]. Also very early band structure calculations of the Be dielectric response function for $\boldsymbol{q} \parallel [001]$ within the RPA by Taut and Hanke [31] have revealed peak positions all in agreement with the experiment.

The situation with Al is somewhat more puzzling. Early IXSS experiments on Al by Platzman and Eisenberger [6] and their repetition with synchrotron radiation [32] revealed a fine structure (peak shoulder with a dip in between) of $S(\boldsymbol{q}, \omega)$ for $q = 1.7k_F$, which seems to be $\boldsymbol{q}$-orientation independent and was attributed in [32] to self-energy effects within the jellium model as calculated 'on the shell' by Múkhopadhyay *et al* [33] in spite of the fact that Ng and Dabrowski [34] have put forward a fundamental objection against the application of the 'on-shell' approximation. Schülke *et al* have interpreted the same fine structure they have found in their IXS spectra of Al [17], and which indeed turned out to be $\boldsymbol{q}$-orientation independent, as being induced by band structure effects, where the dip of this fine structure could not be attributed to only one Bragg plane but interpreted as a consequence of a downshift of d-like unoccupied bands as predicted by Ojala [35]. Band structure $S(\boldsymbol{q}, \omega)$ calculations of Al performed by Maddocks *et al* [36] and Fleszar *et al* [37], both using the time-dependent local density approximation (TDLDA), have clearly revealed this fine structure and have given convincing arguments for their band structure origin. In [36] this fine structure is explicitly assigned to (330) and (040) Bragg planes, so that its $\boldsymbol{q}$-orientation independence becomes understandable. A further hint at the band structure origin of this fine structure has been delivered by Sternemann *et al* [22] by investigating its temperature dependence. The stepwise

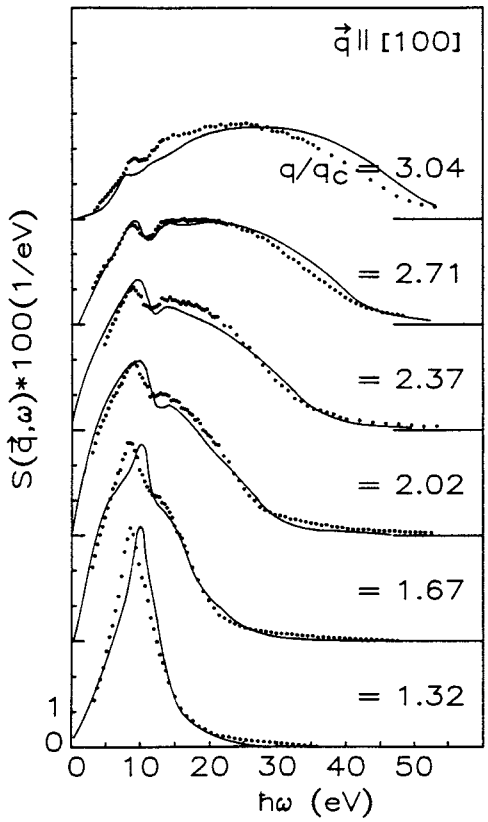

Figure 5. Measured dynamic structure factor $S(\boldsymbol{q}, \omega)$ (points) of Li for $\boldsymbol{q} \parallel [100]$ compared with local empirical pseudopotential calculations; $q_c = 0.46$ a.u.

vanishing of this fine structure with increasing temperature over the melting point is explained as a consequence of a Debye–Waller factor acting on the potential coefficients responsible for the appearance of this structure. Moreover, Maddocks *et al* [36] have found another strongly orientation-dependent dip assigned to a (220) Bragg plane for $\boldsymbol{q} \parallel [110]$ which has also been notified in the IXS spectra of Schülke *et al* [17] for the same $\boldsymbol{q}$-direction. This must be considered as a strong argument in favour of band structure induced fine structure of $S(\boldsymbol{q}, \omega)$ in a nearly free electron metal such as Al. Finally the IXSS measurements on Si [38] should be mentioned, where an excitation gap fine structure was found for $\boldsymbol{q} \parallel [100]$ and could be interpreted as being due to the (220) Bragg plane.

2.3.2. Momentum and energy width of band gaps. The band gap between the valence and conduction band of semiconductors or insulators can also be investigated by IXSS, as shown most recently by Caliebe *et al* [39] in a study on diamond and LiF. This study demonstrates that IXSS can determine the energy width of the gap and, in the case of an indirect gap, also its relative momentum, which is not possible with the conventional optical absorption or reflectivity measurements, since those experiments cannot determine the momentum of the phonon, necessary to observe the indirect gap. Figure 6 shows experimental data of $-\mathrm{Im}\,[1/\varepsilon(\boldsymbol{q}, \omega)]$ of diamond near the band gap as a function of momentum transfer in the ΓX direction along with corresponding calculations, where the full curves take into account the

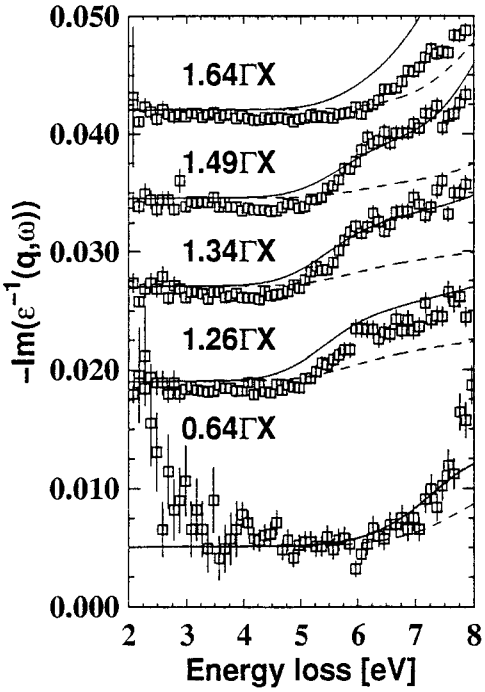

Figure 6. Loss function $-\mathrm{Im}\,[\varepsilon^{-1}(\boldsymbol{q},\omega)]$ of diamond near the band gap as a function of momentum transfer in the ΓX direction. Open squares, experimental data; full curve, calculation including electron–hole interaction in the final state; dashed curve, calculation without electron–hole interaction.

electron–hole interaction (see subsection 2.2.4) and the dashed curves do not [39]. One can clearly see that the gap of 5.5 eV (the minimum of the first rise) is not observed at $q = 0.64\Gamma\mathrm{X}$, as predicted by theory ($0.75\Gamma\mathrm{X}$), but at $1.34\Gamma\mathrm{X}$, which is $q \approx -0.64\Gamma\mathrm{X} + 2\Gamma\mathrm{X}$, where $2\Gamma\mathrm{X}$ is the corresponding reciprocal lattice vector. This behaviour can be explained by taking into account the symmetry of the wavefunction at the valence band maximum and at the conduction band minimum, when calculating the matrix elements in (2.16).

The authors of this study stressed the point that with the availability of synchrotron radiation of fourth generation sources the full information (energy and momentum) about much smaller gaps, as for instance in high-T_c superconductors, should also be feasible although not easy.

2.3.3. Combined density of states (DOS). According to (2.16), each measurement of $S(\boldsymbol{q},\omega)$, done within the range of particle–hole excitation, should give information about the combined density of states (δ-function in (2.16)), of course weighted by the corresponding matrix elements. However, this general property then only leads to pronounced structures of $S(\boldsymbol{q},\omega)$, when the energy difference between the conduction band $E(\boldsymbol{k}',\nu')$ and the valence band $E(\boldsymbol{k},\nu)$ in the δ-function of (2.16) is nearly constant over a wide range of $\boldsymbol{k}$, where $\boldsymbol{k}' = \boldsymbol{k}+\boldsymbol{q}+\boldsymbol{g}$ and $\boldsymbol{g}$ reduces $\boldsymbol{k}+\boldsymbol{q}$ into the first Brillouin zone. Such a case was utilized by Schülke *et al* [40, 41] both to get information about the so-called interlayer conduction band state of graphite [42], the existence of which was difficult to prove with other spectroscopies, and to demonstrate the shift of the interlayer state upon lithium intercalation. Figure 7 shows the IXS spectra of

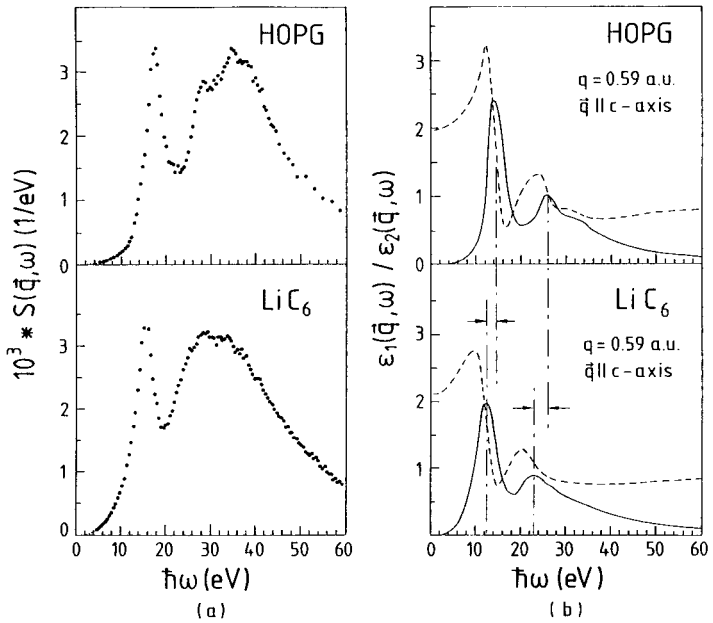

Figure 7. (a) Measured dynamic structure factor $S(\boldsymbol{q}, \omega)$ of HOPG and LiC_6. (b) Corresponding real part, $\varepsilon_1(\boldsymbol{q}, \omega)$ (dashed curve) and imaginary part $\varepsilon_2(\boldsymbol{q}, \omega)$ (full curve) of the dielectric function.

highly oriented pyrolytic graphite (HOPG) and of Li-intercalated HOPG, LiC_6, for $\boldsymbol{q} \| c$-axis, $q = 0.59$ a.u., together with the corresponding real, $\varepsilon_1(\boldsymbol{q}, \omega)$, and imaginary part, $\varepsilon_2(\boldsymbol{q}, \omega)$, of the dielectric function as obtained by Kramers–Kronig analysis of the experimental data. A part of the first peak in the spectra can be attributed, according to selection rules (see the matrix elements in (2.16)), to perpendicular transitions between the π-type valence bands and the σ-type interlayer conduction band, which are nearly parallel over a large range of $\boldsymbol{k} \perp c$-axis. One clearly sees a shift of this structure upon intercalation. This shift is interpreted as being due to a corresponding non-rigid band shift of the interlayer state to lower energies as a consequence of strong hybridization with the Li metal 2s band [43]. A similar study was performed on potassium intercalated graphite KC_8 [44].

2.4. Core excitation with IXSS

It was first pointed out by Mizuno and Ohmura [45] and later by Nagasawa *et al* [46] that the core excitation part of the IXS spectra also contains very useful information about the density of unoccupied and core excitonic states. Since the energy transfer $\hbar\omega$ for core excitations is much larger than the Fermi energy, $|\varepsilon_{RPA}(\boldsymbol{q}, \omega)| \approx 1$ for this range of ω, so that, according to (2.14) and (2.16), $S_{RPA}(\boldsymbol{q}, \omega)$ reads as follows:

$$S_{RPA}(\boldsymbol{q}, \omega) = (\hbar q^2/4\pi e^2 n) \sum_{\boldsymbol{k}', \nu'} |\langle \boldsymbol{k}' \nu' | \exp(\mathrm{i}\boldsymbol{q} \cdot \boldsymbol{r}) | c \rangle|^2 \delta[\hbar\omega + E_c - E(\boldsymbol{k}', \nu')] \tag{2.17}$$

where $|c\rangle$ is the core state with energy E_c. If $qa < 1$, where a is the orbital radius of the core state, the matrix element of (2.17) reduces to the dipole matrix element $\langle \boldsymbol{k}' \nu' | \boldsymbol{r} | c \rangle$, and one ends up with

$$S_{RPA}(\boldsymbol{q}, \omega) = (\hbar q^2/4\pi e^2 n) \left\{ \boldsymbol{q} \cdot \sum_{\boldsymbol{k}', \nu'} |\langle \boldsymbol{k}' \nu' | \boldsymbol{r} | c \rangle|^2 \delta[\hbar\omega + E_c - E(\boldsymbol{k}', \nu')] \cdot \boldsymbol{q} \right\} \tag{2.18}$$

an expression which is equivalent to the cross section of absorption spectroscopy, if one replaces $\boldsymbol{q}$ by the polarization vector $\boldsymbol{e}$ of the absorbed photon. The equivalence between absorption spectroscopy and IXSS was first emphasized in a theoretical study by Mizuno and Ohmura [45] and demonstrated experimentally in [46] by comparing Li and Be core excited IXS spectra with corresponding soft x-ray absorption spectra. Moreover, the strong $\boldsymbol{q}$-orientation dependence of core excited IXSS has been illustrated on HOPG [40].

Therefore, one can obtain, by core excitation IXSS, the same information about the scattering system as in absorption spectroscopy, where the scattering vector $\boldsymbol{q}$ replaces the polarization vector $\boldsymbol{e}$, but with the clear advantage that this information is obtainable with hard x-rays investigating core excitations in the 10–300 eV range. Investigations of the near-edge x-ray absorption fine structure (NEXAFS) and of the extended x-ray absorption fine structure (EXAFS) of low-Z elements with 10–20 keV x-rays become feasible. This was utilized first by Tohji and Udagawa [47] to obtain and to evaluate EXAFS oscillations in graphite. The fine structure of IXS spectra near the Li–K edge in Li intercalated graphite, LiC_6, for $\boldsymbol{q}$ parallel and perpendicular to the axis [48] has been utilized to find the energy position and the symmetry of van-Hove singularities of the unoccupied KC_8 band structure as calculated by Holzwarth *et al* [49], where the so-called interlayer states experience emphasis because of their strong overlap with the Li sites.

Most recently the above-mentioned advantages of core excitation IXSS were utilized in a NEXAFS/EXAFS study of liquid water and ice (Ih) by investigating the O–K edge [50]. The partial distribution function of liquid water was found to be in good agreement with that obtained from elastic neutron scattering. In the near-edge region distinct differences between solid and liquid can be traced back to differences in the local structure and the electronic environment of the oxygen atoms. Schell *et al* [51] demonstrated the potential of core excitation IXSS by investigating the K-edge spectra of solid hcp ^{4}He at 4.3 K and 61.5 MPa. They were able to find for the first time the energy position of the Frenkel-type exciton of atomic parentage related to the transition $1\,^1S_0 \rightarrow 2\,^1P_1$ in the solid state.

The transition from the $qa < 1$ range (dipole approximation) to the $qa > 1$ range, where either monopole or higher than dipole contributions should come into play, has been investigated by Krisch *et al* [52] and Nagasawa *et al* [53]. In both studies, core excitation IXS spectra near the Li–K edge are shown. In [52], as shown in figure 8, the comparison of the spectrum at $qa = 0.176$ with the p-partial DOS demonstrates the predominance of the dipole transition, whereas the spectrum at $qa = 1.95$, together with the s-partial DOS, clearly shows the major contribution of the monopole transition. The high-energy resolution available (ESRF undulator beamline ID16) enabled the authors to fit their experiments to the Mahan, Nozieres and DeDominicis theory [54], so that the angular-dependent parameters α_0 and α_1 were obtained, in good agreement with calculations of Girvin and Hopfield [55]. Thus the long-standing problem of the many-body theory could be solved. In the study [53] the more extended near-edge structure was investigated when passing over from the $qa < 1$ to the $qa > 1$ range. Several models were tested.

2.5. Going beyond RPA

The plasmon features as well as the fine structure of $S(\boldsymbol{q}, \omega)$ due to band structure effects discussed so far could well be explained within the limits of the RPA at least as far as their energy position is concerned. However, it turned out very early on that the overall shapes of the experimental IXS spectra, especially for $q > q_c$, are far from being described adequately by the RPA. Therefore, more sophisticated corrections to the RPA are necessary. Without going through the huge amount of theoretical literature devoted to this problem (reviewed to a large

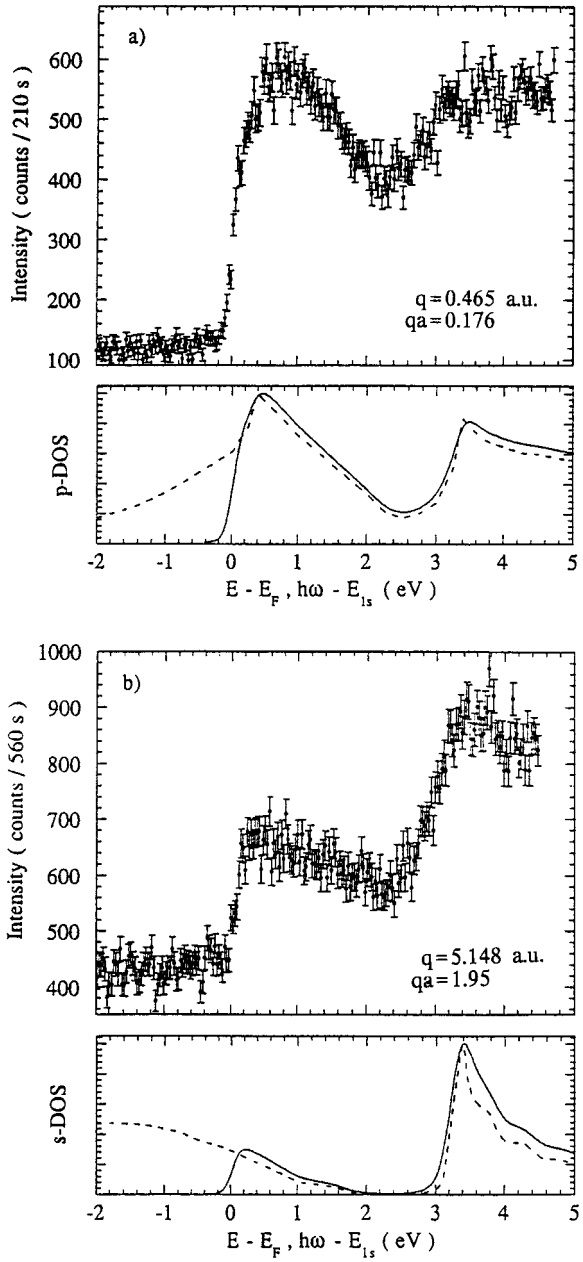

Figure 8. (a) Upper panel: 1s-core excitation IXS spectrum of Li for $q = 0.465$ a.u. Lower panel: Dashed curve, p-partial DOS; full curve, unoccupied p-partial DOS convoluted with the experimental resolution. (b) Upper panel: 1s-core excitation IXS spectrum of Li for $q = 5.148$ a.u. Lower panel: Dashed curve, s-partial DOS; full curve: unoccupied s-partial DOS convoluted with the experimental resolution.

extent in [11]), one can say that two corrections of the simple diagram (bubble) of figure 1 are the most important ones. One correction consists in taking into account the fact that the excited particle or hole can polarize the electron fluid surrounding it, so that this polarization can act

back on the particle or hole thus modifying the particle/hole propagator. Formally this type of reaction is expressed for the jellium case in the so-called self-energy, a complex function of momentum $\boldsymbol{k}$ and energy E given by [56]

$$\Sigma(\boldsymbol{k}, E) = [\mathrm{i}/(2\pi)^4] \int v(\boldsymbol{k}')\, \mathrm{d}^3k' \int \exp(-\mathrm{i}\eta E')\, \mathrm{d}E'/[\varepsilon_{RPA}(\boldsymbol{k}', E')(E - E' - \varepsilon_{\boldsymbol{k}-\boldsymbol{k}'})]$$
$$\eta \to +0 \tag{2.19}$$

if the dynamic screening of the Coulomb interaction is performed via the RPA response function. Allowing for this self-energy, the simple one-particle picture, where the free particle is represented by its momentum and the corresponding kinetic energy $\varepsilon_{\boldsymbol{k}}$, must be modified into a quasi-particle picture, dominated by the so-called spectral density function $A(\boldsymbol{k}, E)$, which expresses for positive (negative) energies E the relative probability per energy unit for the system to be in a state with an energy $E + \mu$ $(-E - \mu)$ above the ground state just after the injection of one electron (hole) of momentum $\boldsymbol{k}$ (μ is the chemical potential) [57]. The spectral density function is connected to the self-energy by

$$A(\boldsymbol{k}, E) = -(1/\pi)\mathrm{Im}\, \Sigma(\boldsymbol{k}, E)/\{[E - \varepsilon_{\boldsymbol{k}} - \mathrm{Re}\, \Sigma(\boldsymbol{k}, E)]^2 + [\mathrm{Im}\, \Sigma(\boldsymbol{k}, E)]^2\} \tag{2.20}$$

so that the imaginary part of the self-energy stands for a broadening of the spectral density function, which is connected with the finite lifetime of the quasi-particle, and the real part of the self-energy characterizes the energy shift relative to the free particle kinetic energy $\varepsilon_{\boldsymbol{k}}$. Thus the definition of the Green's function given in (2.7) must be changed accordingly into

$$G(\boldsymbol{k}, \varepsilon) = (1/2\pi)\left\{ \sum_{-\infty}^{E_F} \mathrm{d}E\, A(\boldsymbol{k}, E)/[\varepsilon - E - \mathrm{i}\eta] + \int_{E_F}^{\infty} \mathrm{d}E\, A(\boldsymbol{k}, E)/[\varepsilon - E + \mathrm{i}\eta] \right\}. \tag{2.21}$$

If we replace the 'undressed' Green's function in the expression (2.6) for the Lindhard polarization function by the self-energy corrected Green's function (2.21) (often designated as fully 'dressed' propagator) we will speak of the fully self-energy corrected polarization function $\chi_{SE}(\boldsymbol{q}, \omega)$.

One can easily show that the imaginary part of $\chi_{SE}(\boldsymbol{q}, \omega)$ is then given by folding the spectral density of the particle with that of the hole left behind:

$$\mathrm{Im}\, \chi_{SE}(\boldsymbol{q}, \omega) = -\int (\mathrm{d}^3k/8\pi^3) \int_{-\omega+E_F}^{E_F} (\mathrm{d}E/2\pi) A(\boldsymbol{k}, E) A(\boldsymbol{k} + \boldsymbol{q}, E + \omega). \tag{2.22}$$

If one neglects the real part of the self-energy and interprets the 'on-shell' imaginary part of the self-energy, $\Gamma/2 \equiv \mathrm{Im}\, \Sigma(\boldsymbol{k}, \varepsilon_{\boldsymbol{k}})$, as the inverse lifetime of the particle with momentum $\boldsymbol{k}$, one can insert $\mathrm{i}\Gamma/2$ into the energy denominator of (2.7). This approximation is called the quasi-particle lifetime model [58], and, in spite of the rather crude approximation, it has been shown in a number of studies that it can bring the calculation nearer to the experiment, when compared with the pure RPA. This has been demonstrated in [11, 17, 22, 33, 38]. In contrast, the exclusive application of the full self-energy correction does not lead to a better agreement with experiment in comparison with RPA [22], and demonstrated in figure 9, where the measured dynamic structure factor of Li [11] for $q \approx 2k_F$ is set against a jellium calculation which includes the full self-energy correction. This is mainly due to the two-peak structure of the hole spectral density function with a so-called plasmaron peak shifted to lower energies against the quasi-hole peak by more than the plasmon energy, as first shown by Lundqvist [59], and discussed in relation to the dynamic structure factor by Ng and Dabrowski [34].

There must exist another correction [60], which acts against the self-energy correction, namely the so-called vertex correction, which takes into account the particle–hole Coulomb interaction dynamically screened by the polarization of the surrounding electron liquid and

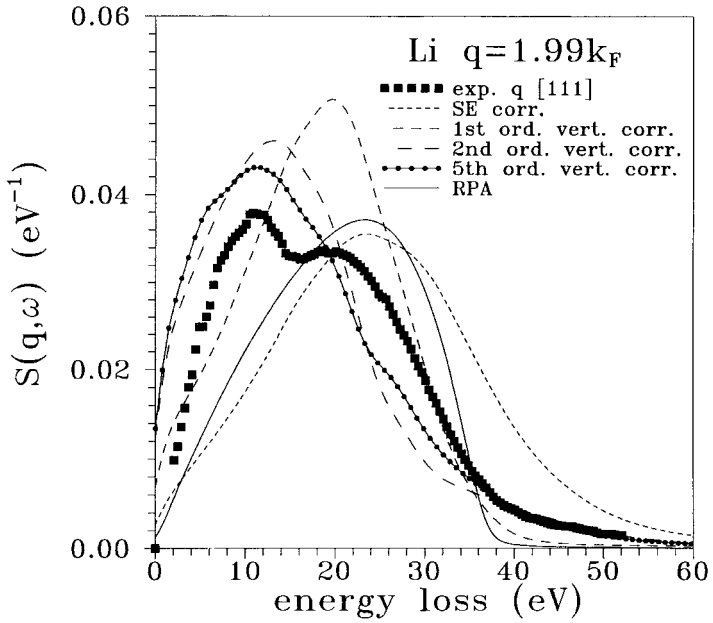

Figure 9. Dynamic structure factor of Li with $q = 1.99k_F$. Full squares: experiment with $\boldsymbol{q} \parallel [111]$, normalized according to the f-sum rule [11]; short dashed curve, jellium calculation including full self-energy correction performed by means of a cumulant expansion [63]; dashed curves, jellium calculation, fully self-energy corrected and vertex correction to first and second order in the screened Coulomb interaction, respectively; full curve with full circles, jellium calculation, fully self-energy corrected and vertex corrected to the fifth order in the screened Coulomb interaction; full curve, jellium calculation within RPA without self-energy and vertex correction.

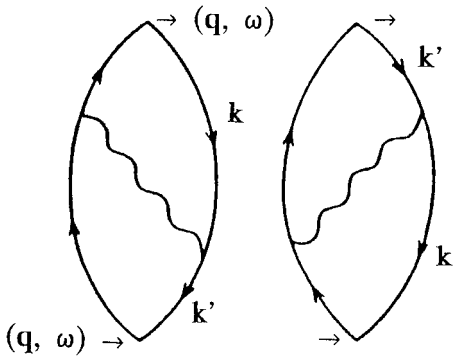

Figure 10. Diagrams representing the first-order vertex correction of the fully self-energy corrected polarization function. The propagators are 'dressed' one-particle Green's functions.

which is, to first order in the Coulomb interaction, diagrammatically shown in figure 10. The corresponding expression of the first-order vertex correction to $\chi_{SE}(\boldsymbol{q}, \omega)$ reads as follows:

$$\Delta_l^{vert}\chi(\boldsymbol{q},\omega) = -2\int \mathrm{d}^3k/(8\pi^3)\int \mathrm{d}\varepsilon/(2\pi\mathrm{i})G(\boldsymbol{k},\varepsilon)G(\boldsymbol{k}+\boldsymbol{q},\varepsilon+\omega)\int \mathrm{d}^3k'/(8\pi^3)$$
$$\times\int \mathrm{d}\varepsilon'/(2\pi\mathrm{i})[v(\boldsymbol{k}'-\boldsymbol{k})/\varepsilon_{RPA}(\boldsymbol{k}'-k,\varepsilon'-\varepsilon)]G(\boldsymbol{k}',\varepsilon')G(\boldsymbol{k}'+\boldsymbol{q},\varepsilon'+\omega). \tag{2.23}$$

It has been shown by Sternemann *et al* [61] in a Li IXSS experiment that, at least for $q > 2k_F$, this first-order vertex correction not only cancels the self-energy correction, but brings the calculation in good agreement with experiment. A cancellation of this type has been discussed explicitly for the case of optical absorption by Beeferman and Ehrenreich [62] and for the dynamic structure factor by Green *et al* [58]. However, allowing for the vertex correction to higher orders in the screened Coulomb potential (simply by adding further virtual plasmon exchange channels into the polarization 'bubble' of figure 1) leads also for $q \approx 2k_F$ to a rather good agreement with the experiment, as shown in figure 9 for Li, provided that the spectral density function of (2.20), as used in (2.21), is replaced by one obtained by means of a cumulant expansion treatment [63]. The position of the main peak at 11.5 eV is well reproduced and the tail of the spectrum between 36 and 52 eV, in particular, is in perfect agreement with the experiment. The latter agreement was also found by Sturm and Gusarov [64] for the case of Al using a diagrammatic expansion of the polarization function as proposed by Geldart and Vosko [65]. Of course, diagrams of the above-mentioned type are not the only ones contributing to the polarization function (see for further diagrams [58]), so that a full agreement with experiment cannot be expected. The shoulder around 19.5 eV in the experimental spectrum could be attributed to lattice effects comparable with the Al case [17, 36, 37].

If one replaces the screened Coulomb interaction [. . .] in (2.23) formally by $G(\boldsymbol{q}, \omega)v(\boldsymbol{q})$, the vertex correction to all orders of the Coulomb potential can be summed up in a geometrical series, ending up with the so-called local-field corrected polarization function

$$\chi_{LF}(\boldsymbol{q}, \omega) = \chi_{SE}(\boldsymbol{q}, \omega)/[1 + G(\boldsymbol{q}, \omega)v(\boldsymbol{q})\chi_{SE}(\boldsymbol{q}, \omega)] \tag{2.24}$$

where the complex function $G(\boldsymbol{q}, \omega)$ should be designated as dynamic local-field correction function (LFCF), whose static approximation was first introduced by Hubbard [66]. A great deal of theoretical work has been invested in finding expressions of the static LFCF $G(\boldsymbol{q}, 0)$ for homogeneous systems, reviewed by Kugler [67]. An analytical expression for $G(\boldsymbol{q}, 0)$, which is widely used in the literature, has been provided by Utsumi and Ichimaru [68]. It has been shown in [11, 17, 22, 38] that by using these expressions for $G(\boldsymbol{q}, 0)$, together with the quasi-particle lifetime model, one gets, at least for $q \leqslant k_F$, good agreement between the overall shape of the experimental IXS spectra and the corresponding calculations. For larger q, a deviation came up, so it was natural to use (2.24) to fit $G(\boldsymbol{q}, \omega)$ to the experiment. The result of such a fit, performed by Schülke *et al* [69], is presented in figure 11, where $\bar{\omega}$ in the argument of G denotes the centre of a frequency range $\bar{\omega} \pm \Delta\omega$ chosen for the fit. The fitted LFCF is compared with theoretical values both of [68] and of Farid *et al* [70] using different values for the renormalization constant z [18]. Another approach to implementing the local-field correction for the case of Al into calculations of the polarization function, when band structure effects should be taken into account, was chosen by Maddocks *et al* [36] and Fleszar *et al* [37]. These authors have shown that application of TDLDA is equivalent to making a static local-field correction. Indeed, by using this scheme, the authors could get a much better agreement with experiment than with RPA. Larson *et al* [71] have carried on these studies and found out that for $q > k_F$ agreement with experiment could only be obtained by fitting empirical LFCFs to the experimental data ending up with values comparable with that of [69]. Finally it should be mentioned that Benedict and Shirley [72] have introduced a first-principle scheme to calculate the dielectric response of insulators, which includes the electron–hole interaction, where the effective Hamiltonian for electron–hole pairs contains both the exchange and the direct part of this interaction. It was shown in [39] that the application of this scheme to LiF and diamond leads to much better agreement with experiment when compared with calculations which neglect electron–hole interactions.

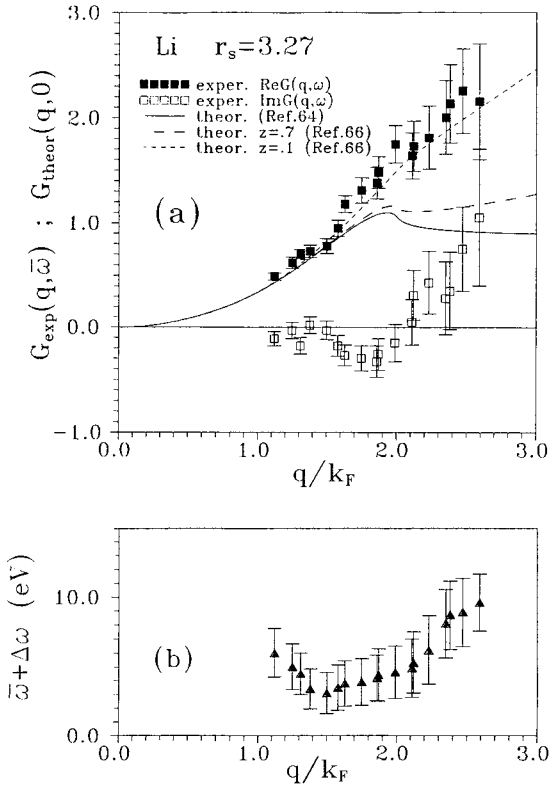

Figure 11. (a) Real and imaginary parts of the LFCF $G(\boldsymbol{q}, \omega)$: data points represent real and imaginary parts of $G_{exp}(q, \bar{\omega})$ as fitted, within a certain range around $\bar{\omega}$ to the experiment; lines represent $G_{theor}(\boldsymbol{q}, 0)$ according to different approaches as indicated. (b) Frequency range of fit.

3. Non-resonant IXSS, off-diagonal response

3.1. Basic relations

The relation (2.4), which defines the polarization function $\chi(\boldsymbol{q}, \omega)$ for an homogeneous electron system, must be modified if we fully take into account the lattice translational symmetry, so that the electron density can be expanded into the following Fourier series:

$$n(\boldsymbol{r}) = \sum_{\boldsymbol{g}} n(\boldsymbol{g}) \exp(\mathrm{i}\boldsymbol{r} \cdot \boldsymbol{g}). \tag{3.1}$$

Doing so has the consequence that a Fourier component of the external potential, $\phi_{ext}(\boldsymbol{q}_r + \boldsymbol{g}', \omega)$, can also induce density fluctuations belonging to another reciprocal lattice vector $\boldsymbol{g}$, where $\boldsymbol{q}_r$ reduces the wavevector $\boldsymbol{q}$ into the first Brillouin zone according to

$$\boldsymbol{q} = \boldsymbol{q}_r + \boldsymbol{g}'. \tag{3.2}$$

In this way the polarization function changes into a $(\boldsymbol{g}, \boldsymbol{g}')$-matrix, defined by [69, 70]

$$n_{ind}(\boldsymbol{q}_r + \boldsymbol{\omega}) = -e\chi(\boldsymbol{q}_r + \boldsymbol{g}, \boldsymbol{q}_r + \boldsymbol{g}', \omega)\phi_{ext}(\boldsymbol{q}_r + \boldsymbol{g}', \omega). \tag{3.3}$$

According to (2.13) the RPA dielectric function changes into a dielectric matrix

$$\varepsilon(\boldsymbol{q}_r + \boldsymbol{g}, \boldsymbol{q}_r + \boldsymbol{g}', \omega) \equiv \varepsilon_{gg'}(\boldsymbol{q}_r, \omega) = \delta_{gg'} + T_{gg'} \tag{3.4}$$

where [73, 74]

$$T_{gg'} = [8\pi e^2/(\boldsymbol{g}+\boldsymbol{q})^2 V] \sum_{\substack{\boldsymbol{k},\nu \\ \boldsymbol{k}',\nu'}} \langle \boldsymbol{k}\nu | \exp[-\mathrm{i}(\boldsymbol{q}+\boldsymbol{g})] \cdot \boldsymbol{r} | \boldsymbol{k}'\nu' \rangle \langle \boldsymbol{k}'\nu' | \exp[\mathrm{i}(\boldsymbol{q}+\boldsymbol{g}') \cdot \boldsymbol{r}] \boldsymbol{k}, \nu \rangle$$
$$\times [f(\boldsymbol{k}', \nu') - f(\boldsymbol{k}, \nu)]/[\hbar\omega + E(\boldsymbol{k}, \nu) - E(\boldsymbol{k}', \nu') + \mathrm{i}\eta] \qquad \eta \to +0. \quad (3.5)$$

By performing an inelastic scattering experiment, where the scattering of a single plane wave will transfer only one momentum $\boldsymbol{q}$ to the scattering electron system, the corresponding macroscopic response function $\varepsilon^{-1}(\boldsymbol{q}, \omega)$ must read as follows:

$$\varepsilon^{-1}(\boldsymbol{q}, \omega) = [\varepsilon_{gg'}(\boldsymbol{q}_r, \omega)]^{-1}_{g'g'} \quad (3.6)$$

$\varepsilon^{-1}(\boldsymbol{q}, \omega)$ is directly related to the $\boldsymbol{g}'\boldsymbol{g}'$-diagonal element of the inverted dielectric matrix, so that one can define a diagonal structure factor

$$S(\boldsymbol{q}_r + \boldsymbol{g}', \omega) = [-\hbar(\boldsymbol{q}_r + \boldsymbol{g}')^2/4\pi^2 e^2 n] \mathrm{Im}\, \{[\varepsilon_{gg'}(\boldsymbol{q}_r, \omega)]^{-1}_{g'g'}\} \quad (3.7)$$

which replaces the RPA structure factor as given in (2.14). Speaking in terms of physical intuition, one can express the diagonal response function as being proportional to the modulus squared of $a(\boldsymbol{q}_r + \boldsymbol{g}', \omega)$,

$$-\mathrm{Im}\, \{[\varepsilon_{gg'}(\boldsymbol{q}_r, \omega)]^{-1}_{g'g'}\} \sim |a(\boldsymbol{q}_r + \boldsymbol{g}', \omega)|^2 \quad (3.8)$$

where $a(\boldsymbol{q}_r + \boldsymbol{g}', \omega)$ is the probability amplitude to excite the system by transferring the energy $\hbar\omega$ and the momentum $\boldsymbol{q} = \boldsymbol{q}_r + \boldsymbol{g}'$.

Accordingly one can write down an off-diagonal structure factor

$$S(\boldsymbol{q}_r + \boldsymbol{g}', \boldsymbol{q} + \boldsymbol{g}, \omega) = [-\hbar(\boldsymbol{q}_r + \boldsymbol{g}')^2/4\pi^2 e^2 n] \mathrm{Im}\, \{[\varepsilon_{gg'}(\boldsymbol{q}_r, \omega)]^{-1}_{gg'}\} \quad (3.9)$$

where the off-diagonal response function

$$-\mathrm{Im}\, \{[\varepsilon_{gg'}(\boldsymbol{q}_r, \omega)]^{-1}_{g'g'}\} \sim a(\boldsymbol{q}_r + \boldsymbol{g}, \omega) a^*(\boldsymbol{q}_r + \boldsymbol{g}', \omega) \quad (3.10)$$

is related to the product of two excitation probability amplitudes belonging to two different transferred momenta, namely $\boldsymbol{q}_r + \boldsymbol{g}$ and $\boldsymbol{q}_r + \boldsymbol{g}'$.

3.2. Experimental access to off-diagonal response

It has been shown by Schülke [75, 76] that one can get information about off-diagonal response by performing an inelastic x-ray scattering experiment, where the incident photon state consists of the coherent superposition of two plane waves with wavevector $\boldsymbol{K}_0$ and amplitude A_0, on the one hand, and another with wavevector $\boldsymbol{K}_h = \boldsymbol{K}_0 + \boldsymbol{g}$ and amplitude A_h as sketched in figure 12. If one observes the scattered radiation with wavevector $\boldsymbol{K}'$ and frequency ω', one has indeed two transferred momenta $\boldsymbol{q}_0 = \boldsymbol{K}_0 - \boldsymbol{K}'$ and $\boldsymbol{q}_h = \boldsymbol{K}_h - \boldsymbol{K}'$. One can easily show that the coherent coupling of these two incident plane wave components leads to a corresponding coherent coupling (quantum interference) of the related excitation probability amplitudes $a(\boldsymbol{q}_0, \omega)$ and $a(\boldsymbol{q}_h, \omega)$ according to the following expression for the DDCS either in terms of the excitation probability amplitudes or in terms of the diagonal and off-diagonal structure factors:

$$\mathrm{d}^2\sigma/\mathrm{d}\Omega\, \mathrm{d}\omega' \sim |A_0|^2 |a(\boldsymbol{q}_0, \omega)|^2 + |A_h|^2 |a(\boldsymbol{q}_h, \omega)|^2$$
$$+ A_0 A_h^* a(\boldsymbol{q}_0, \omega) a^*(\boldsymbol{q}_h, \omega) + A_0^* A_h a^*(\boldsymbol{q}_0, \omega) a(\boldsymbol{q}_h, \omega) \quad (3.11)$$

$$\mathrm{d}^2\sigma/\mathrm{d}\Omega\, \mathrm{d}\omega' \sim (|A_0|^2 + |A_h|^2) S(\boldsymbol{q}_r + \boldsymbol{g}', \omega)|$$
$$+ 2|A_0||A_h| \cos(\Delta\phi) S(\boldsymbol{q}_r + \boldsymbol{g}', \boldsymbol{q}_r + \boldsymbol{g}, \omega). \quad (3.12)$$

The last equation is written down for the special case that $|\boldsymbol{q}_0| = |\boldsymbol{q}_h|$ and that $\boldsymbol{q}_0$ and $\boldsymbol{q}_h$ are symmetry equivalent. $\Delta\phi$ is the phase difference between the two plane wave components.

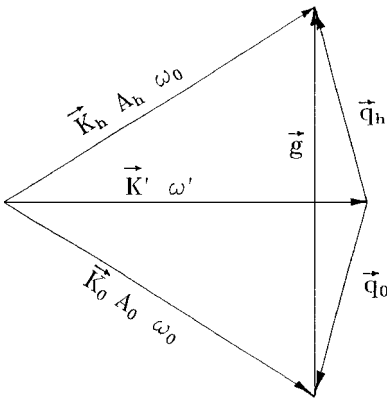

Figure 12. Momentum transfer of an IXSS experiment using two coherently coupled incident waves.

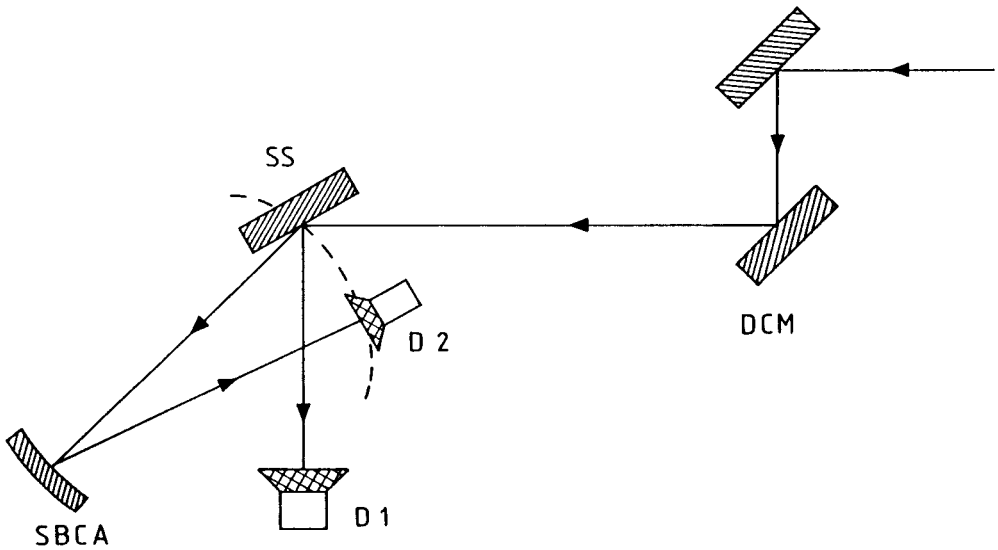

Figure 13. Experimental set-up for a CIXSS experiment: DCM = double crystal monochromator; SS = scattering sample; SBCA = spherically bent crystal analyser; D1 = monitor detector; D2 = detector of the analyser.

In a real experiment, as performed according to figure 13 on Si [77], the two plane waves are components of the electric field as predicted by the dynamical theory of x-ray diffraction [78] within the limits of the so-called two-beam case of diffraction. Their amplitudes A_0, A_h and also their mutual phase shift $\Delta\phi$ depend on the angular deviation $\Delta\theta$ from the exact Bragg position, so that $\Delta\phi$ can be monitored by the Bragg-reflected intensity as shown in figure 13. In particular $\Delta\phi$ goes from 0 to π, when turning the angular sample position by the Darwin width, which is a few μrad, so that the quantum interference term in (3.11) and (3.12) changes its sign. This enables us to extract the excitation probability amplitudes $a(\boldsymbol{q}_0, \omega)$ and $a(\boldsymbol{q}_h, \omega)$ by measuring $\mathrm{d}^2\sigma/\mathrm{d}\Omega\,\mathrm{d}\omega'$ for a few angular positions of the sample within the Darwin width and makes the basis of coherent inelastic x-ray scattering spectrocopy (CIXSS).

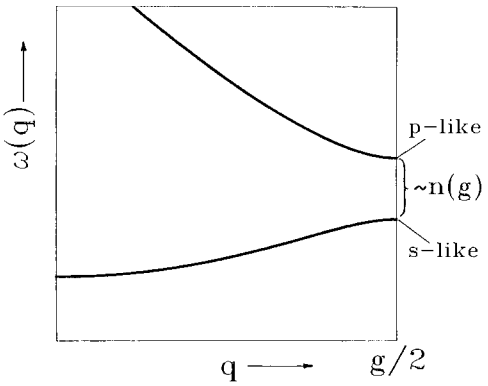

Figure 14. Plasmon band gap at the BZB.

3.3. Measurement of the plasmon band gap

In [77] CIXSS has been applied to the problem of getting information about the plasmon band gap of Si, as predicted by Saslow and Reiter [74], especially about the plasmon band gap of Si at the $\boldsymbol{g} = (2\pi/a)(1, 1, 1)$ Brillouin zone boundary (BZB), whose magnitude has been estimated [79, 80] to be proportional to $n(\boldsymbol{g})$ (see equation (3.1)). If the plasmon band structure at the BZB looks as shown in figure 14 (two-plasmon band model) the diagonal response part of the DDCS for a momentum transfer $\boldsymbol{q} = \boldsymbol{g}/2$ is composed of two contributing squared excitation amplitudes with energy ω_1 and ω_2, each for one plasmon band, according to

$$S(\boldsymbol{q}_r + \boldsymbol{g}', \omega) = |a(\boldsymbol{q}_r + \boldsymbol{g}', \omega)|^2 \delta(\omega - \omega_1(\boldsymbol{q}_r + \boldsymbol{g}')) + |a(\boldsymbol{q}_r + \boldsymbol{g}', \omega)|^2 \delta(\omega - \omega_2(\boldsymbol{q}_r + \boldsymbol{g}')). \tag{3.13}$$

The off-diagonal response part of the DDCS (which can be separated from the diagonal part as shown above) is composed of the two interference terms, one taken at $\omega = \omega_1$, which is positive, since the corresponding plasmon state is s-like, and the other one taken at $\omega = \omega_2$, which is negative, since the corresponding plasmon state is p-like:

$$\begin{aligned} S(\boldsymbol{q}_r + \boldsymbol{g}', \boldsymbol{q}_r + \boldsymbol{g}, \omega) = {} & a^*(\boldsymbol{q}_r + \boldsymbol{g}', \omega) a(\boldsymbol{q}_r + \boldsymbol{g}, \omega) \delta(\omega - \omega_1(\boldsymbol{q}_r + \boldsymbol{g}')) \\ & + a(\boldsymbol{q}_r + \boldsymbol{g}', \omega) a^*(\boldsymbol{q}_r + \boldsymbol{g}, \omega) \delta(\omega - \omega_2(\boldsymbol{q}_r + \boldsymbol{g}')). \end{aligned} \tag{3.14}$$

Thus, for $q = g/2$, one ends up [81] with an s-like (lower) plasmon band, whose excitation probability is given by

$$|a_l(\boldsymbol{g}/2, \omega)|^2 \sim 1/2[S(\boldsymbol{q}_r + \boldsymbol{g}', \omega) + S(\boldsymbol{q}_r + \boldsymbol{g}', \boldsymbol{q}_r + \boldsymbol{g}, \omega)] \tag{3.15}$$

and a p-like (upper) plasmon band, whose excitation probability is given by

$$|a_u(\boldsymbol{g}/2, \omega)|^2 \sim 1/2[S(\boldsymbol{q}_r + \boldsymbol{g}', \omega) - S(\boldsymbol{q}_r + \boldsymbol{g}', \boldsymbol{q}_r + \boldsymbol{g}, \omega)] \tag{3.16}$$

This situation is plotted in figure 15, where one can read both a plasmon gap of ~1 eV and the interesting fact that the lower plasmon band is broader than the upper plasmon band, opposite to what one might expect in terms of plasmon damping, but in good agreement with predictions of Daling *et al* [82]. It should be stressed that signatures of this plasmon gap could not be found in a regular IXSS or EELS experiment, since the Si plasmons, even for $q < q_c$ (q_c = plasmon cut-off vector), are strongly damped due to interband transitions, so that their width is of the order of 5 eV.

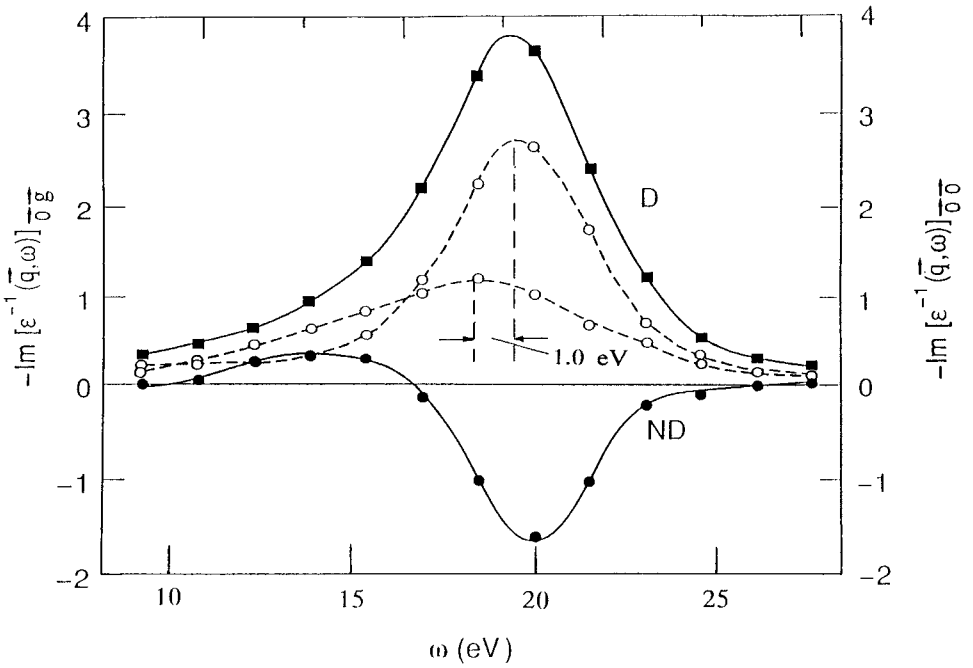

Figure 15. Full squares, diagonal (D) response function $-\mathrm{Im}\,[\varepsilon^{-1}(\boldsymbol{q},\omega)]_{\mathbf{00}}$; full circles, off-diagonal (ND) response function $-\mathrm{Im}\,[\varepsilon^{-1}(\boldsymbol{q},\omega)]_{\mathbf{0}g}$, both measured with $\boldsymbol{q} = \boldsymbol{g}_{111}/2$; open circles connected by dashed curves, lower plasmon band (D+ND)/2, and upper plasmon band (D−ND)/2 separated by 1 eV.

3.4. Plasmon Fano resonances

The existence of Umklapp processes, which lead to plasmon bands, can be proved in another inelastic scattering experiment, where one is utilizing the interaction of the *discrete* Umklapp plasmons, as shown in figure 16 for the repeated zone scheme of a simple two-plasmon band model, with the continuum of particle–hole excitations in the q-range with $q > q_{ZB}$ (q_{ZB} = momentum belonging to the BZB). For general physical reasons such an interaction between discrete excitations and a continuum of excitations should give rise to so-called Fano resonances [83]. This can be demonstrated within the limits of a simple two-plasmon band model, where the dielectric matrix of (3.4) and (3.5) reduces to a 2×2 matrix by taking into account only one reciprocal lattice vector $\boldsymbol{g} \neq \mathbf{0}$, so that $S(\boldsymbol{q},\omega)$ can be expressed in the following way for $\boldsymbol{g}' = \mathbf{0}$ [80]:

$$S(\boldsymbol{q},\omega) = (\hbar q^2/4\pi^2 e^2 n)\mathrm{Im}\,\{(-1/\varepsilon_{gg}) + (\varepsilon_{g\mathbf{0}}\varepsilon_{\mathbf{0}g}/\varepsilon_{gg}^2)[-\varepsilon^{-1}(\boldsymbol{q},\omega)]_{\mathbf{00}}\} \quad (3.17)$$

(the arguments of ε_{gg} and $\varepsilon_{g\mathbf{0}}$ are suppressed).

This expression consists of two parts in the { } brackets. The first one represents the particle–hole excitation spectrum in the range of the Umklapp plasmon. The second one stands for the plasmon coupled to the particle–hole excitation by the factor $\varepsilon_{g\mathbf{0}}\varepsilon_{\mathbf{0}g}/\varepsilon_{gg}^2$, which is complex with negative real and imaginary parts. Since $\mathrm{Im}\,[-\varepsilon^{-1}(\boldsymbol{q},\omega)]_{\mathbf{00}}$ is always positive and $\mathrm{Re}\,[-\varepsilon^{-1}(\boldsymbol{q},\omega)]_{\mathbf{00}}$ becomes negative for $\omega > \omega_p(\boldsymbol{q})$ (ω_p = plasmon frequency), this coupling term exhibits a valley–peak structure, typical for a Fano resonance. This valley–peak structure superimposed on the well known particle–hole contribution was indeed found in $S(\boldsymbol{q},\omega)$ measurements of Si with $\boldsymbol{q} \parallel [111]$ and $q > q_c$ around 18 eV [38, 84] (see figure 17),

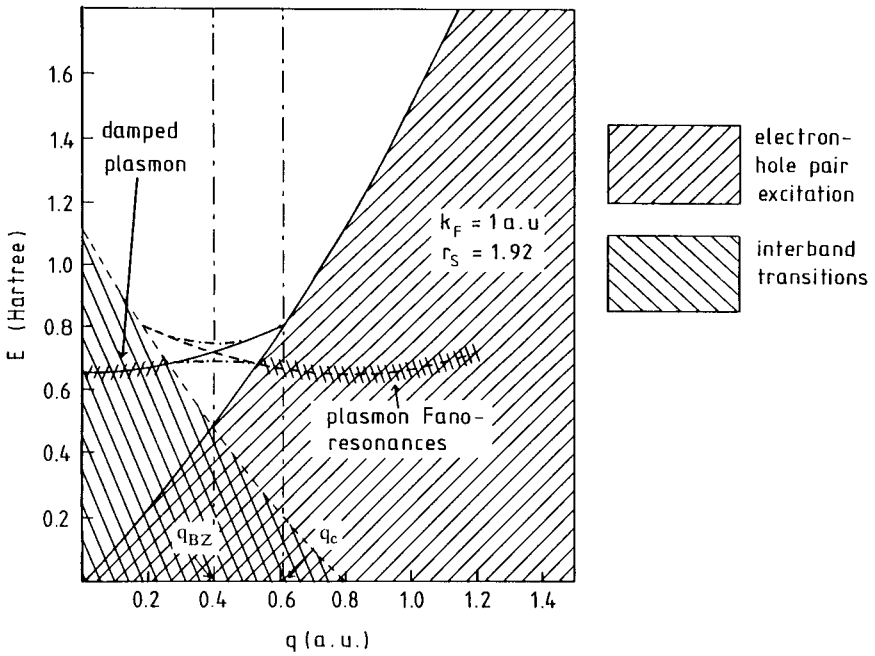

Figure 16. Plasmon band and electron–hole excitation continuum in the repeated zone scheme. q_{BZ} marks the Brillouin zone boundary, q_c = plasmon cut-off vector.

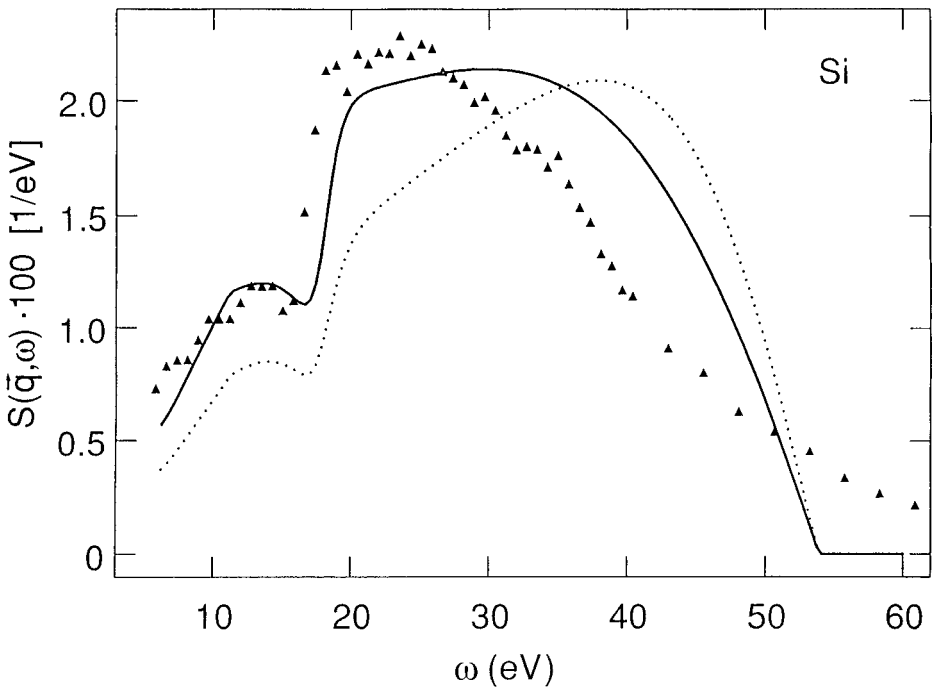

Figure 17. Dynamic structure factor $S(q, \omega)$ of Si for $q \parallel [111]$, $q = 1.25$ a.u. triangles, measurement; dotted curve, two-plasmon-band model calculation within RPA; full curve, two-plasmon-band calculation, local-field corrected.

and of Li with $\boldsymbol{q} \parallel [110]$ and $q > q_c$ [85], where the latter measurements were compared with calculations of the full dielectric matrix [86].

4. Resonant inelastic x-ray scattering (RIXS)

4.1. Basic relations

The relation between the DDCS and the dynamic structure factor, as given in equation (2.1), is only valid as long as the incident energy is far from the binding energy of a core level. If the incident energy is approaching such a binding energy, a second term of the DDSC, deduced from the $\boldsymbol{p}\cdot\boldsymbol{A}$ term ($\boldsymbol{A}$ is the vector potential operator) of the interaction Hamiltonian, becomes dominant, so that the DDSC reads [87]

$$\mathrm{d}^2\sigma/\mathrm{d}\Omega\,\mathrm{d}\omega_2 \sim \sum_f \left| \sum_m \frac{\langle f|\boldsymbol{e}_2^* \cdot \sum_j \boldsymbol{p}_j \exp(-\mathrm{i}\boldsymbol{K}_2 \cdot \boldsymbol{r}_j)|m\rangle\langle m|\boldsymbol{e}_1 \cdot \sum_j \boldsymbol{p}_j \exp(\mathrm{i}\boldsymbol{K}_1 \cdot \boldsymbol{r}_j)|\mathrm{i}\rangle}{E_m - E_i - \hbar\omega_1 - \mathrm{i}\Gamma_m/2} \right|^2 \times \delta(E_f - E_i - \hbar\omega) \tag{4.1}$$

where $|i\rangle$, $|f\rangle$ and $|m\rangle$ are the initial, final and an intermediate state of the scattering electron system, respectively, with their corresponding energies E_i, E_f and E_m, as sketched in figure 18. Γ_m^{-1} is the lifetime of the intermediate state. $\boldsymbol{K}_1, \omega_1, \boldsymbol{e}_1$ and $\boldsymbol{K}_2, \omega_2, \boldsymbol{e}_2$ are the wavevectors, frequencies and polarization vectors of the incident and the scattered wave, respectively, $\omega = \omega_1 - \omega_2$. The summation j is over all electrons of the system.

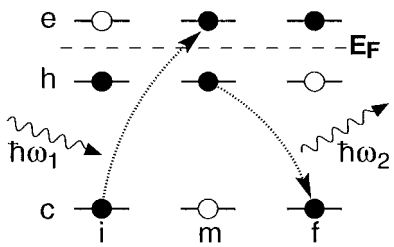

Figure 18. Principle of resonant inelastic scattering.

Let the intermediate state $|m\rangle$ be a core hole with an excited electron in a quasi-continuum of unoccupied states, and let the state $|f\rangle$ be a hole in occupied valence or core states. Then the interplay of the δ-function and the denominator of equation (4.1) shifts the energy of the scattered photon to higher energies with increasing energy of the incident photon, due to the finite lifetime Γ_m^{-1}, where the shift depends linearly on the incident photon energy as long as $\hbar\omega_1 < E_B$ (E_B = binding energy of the core electron involved in $|m\rangle$) and levels out for $\hbar\omega_1 > E_B$. This shift is called the Raman shift and was found experimentally for the first time by Eisenberger *et al* [13]. If, on the other hand, $|m\rangle$ is discrete, the linear Raman shift persists over the whole range of the incident photon energy. Of course, the spectral contribution of this discrete state $|m\rangle$ to the DDSC is modulated by the denominator of equation (4.1).

This property of RIXS can be utilized to measure Γ_m, the core-hole lifetime and to emphasize the contributions of transitions $|i\rangle \Rightarrow |m\rangle$ to the photon absorption cross section, which are too weak to be detectable in conventional x-ray absorption spectroscopy (XAS). Examples for these applications of RIXS are presented in subsection 4.2.

Equation (4.1) forces one to consider the absorption and the re-emission processes involved as an undivided inelastic scattering process, where the initial and final states of the scattering

electron system are the same as in a corresponding non-resonant inelastic scattering process, but where the information about the participating electronic excitation, readable from the DDSC, can be amplified by several orders of magnitude, as compared with non-resonant scattering, due to the resonance denominator. A very important consequence of the coherence of absorption and re-emission consists in the fact that momentum conservation holds for the whole inelastic scattering process as first shown in [88, 89], so that RIXS can be used for band structure determination. Examples for this application of RIXS will be shown in subsection 4.3. However, besides momentum conservation, the conservation of spin can also be claimed, which enables spin selective investigation of the unoccupied band structure by utilizing an internal spin reference, as shown for the first time by Hämäläinen *et al* [90]. Examples of this application of RIXS will be offered in subsection 4.4. Finally, it must be stressed that shakeup excitations can occur from $|m\rangle$, which lead to very interesting energy loss spectra enhanced by resonance, as exemplified in subsection 4.5.

4.2. Core-level resonant Raman spectra

It was shown for the first time by Hämäläinen *et al* [91] that the cross section for a resonantly excited KL transition (initial hole in the K-shell), which is derived by integrating the DDSC of (4.1) with respect to ω_2, and which can be measured by tuning the incident photon energy across the K-edge, is given by

$$(\mathrm{d}\sigma/\mathrm{d}\Omega)_{KL} = [(E_K + \omega_e)/4\pi^2\hbar\omega_1]\sigma_K(E_K + \omega_e)\tan^{-1}(\Gamma_K/2\Delta E) \qquad (4.2)$$

where E_K is the K-shell binding energy, ω_e is the average energy of the ejected electron, σ_K is the K-shell contribution to the photoelectric absorption, ΔE is the incident energy relative to the K-edge ($\Delta E = E_K - \hbar\omega_1$) and Γ_K is the K-shell hole width. The latter quantity can experimentally be determined by utilizing (4.2): one has to measure the scattered intensity into a scattering angle of nearly 90° by means of a solid-state detector, which integrates over the energy distribution of the K_{α^-} and K_{β^-} emission, turning the incident photon energy with an energy width of ∼1 eV across the K-edge. The incident photons should be highly linearly polarized (synchrotron radiation) in order to suppress, together with the 90° scattering angle, the non-resonant scattering. In this way, Γ_K of Cu, Zn and $\Gamma_{L_{III}}$ of Ho [91] and $\Gamma_{L_{III}}$ of Yb and Ta [92] were determined with an accuracy of 0.1 eV.

It was first demonstrated by Hämäläinen *et al* [93] that by using a selected wavelength of the resonantly scattered (re-emitted) radiation as a signal, which indicates the strength of the absorption process when scanning the incident photon energy across an edge, the edge spectra with their information about the density of unoccupied states are free from the influence of the lifetime broadening of the excited core level. The total energy resolution of this type of edge spectroscopy depends only on the energy resolution of the monochromator for the incident beam, the energy resolution of the analyser and the lifetime of the core hole involved in the re-emission process. This remarkable fact is again, like the Raman shift, a consequence of the interplay of the δ-function and the denominator in (4.1).

If one performs, in each case for one incident photon energy below the excited core-level binding energy, an energy analysis of the complete spectrum of the resonantly scattered radiation originating from the re-emission from a core level, then these spectra often reveal a multi-peak structure. Each peak can be attributed to the excitation into a certain set of unoccupied levels of the conduction band, and due to their individual Raman shift the energy distances of these peaks are equal to the differences of the corresponding excitation energies. The intensity of each peak goes through resonance if the incident energy just reaches the excitation energy of the corresponding set of unoccupied levels. Thus the trace of rather weak

excitations as for instance quadrupolar excitations, which are not visible as distinct structures in conventional absorption spectroscopy, can be found, as first demonstrated by Krisch *et al* [94], who found evidence for a quadrupolar excitation channel at the L_{III}-edge of gadolinium, which is not detectable in the conventional x-ray absorption spectroscopy. A more extensive study of this quadrupolar channel at the L_{III}-edge of a series of rare earth compounds has been performed by Bartolome *et al* [95]. As an example of such a series of multi-peak spectra of inelastically scattered photons, the $K_{\alpha_1^-}$ spectra of Cu in CuO for incident photon energies between 8977 and 8984 eV, all below the K-shell binding energy of Cu, $E_K = 8985$ eV, are presented in figure 19 [96]. The peak at the highest energy of the scattered photons can be attributed to a quadrupolar 1s $\rightarrow$ 3d transition and shows resonance at $E_0 = 8979.5$ eV. The other two peaks are due to dipolar transitions to the $\underline{1s}3d^9 4p$ and to the charge transfer state $\underline{1s}3d^{10}\underline{L}4p$, where $\underline{1s}$ and $\underline{L}$ denote a core hole and an oxygen ligand hole, respectively.

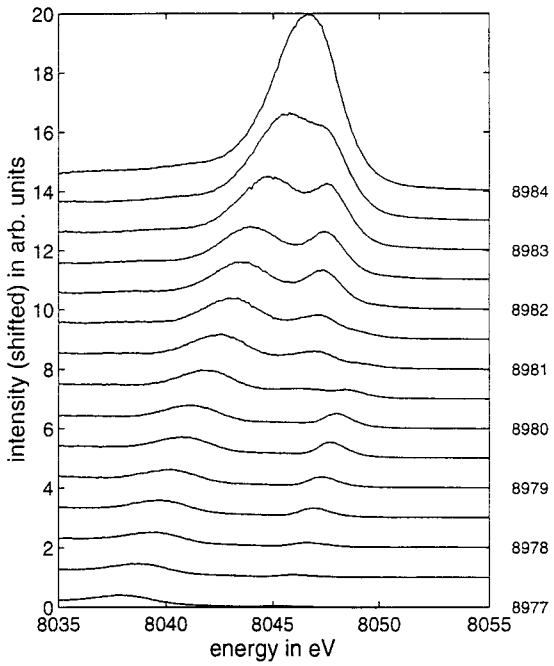

Figure 19. Cu K_{α_1} fluorescence spectra of Cu for increasing excitation energies as indicated (in eV), all below the Cu K-shell binding energy (8985 eV).

4.3. Bloch-k selective RIXS

As first shown by Johnson and Ma [89] on diamond and by Miyano *et al* [97] on Si, in both cases in the soft x-ray regime, and by Enkisch *et al* [98] on NiAl alloy in the hard x-ray regime, the shape of the resonantly excited valence fluorescence spectra from single crystals strongly depends on both the energy of the incident photons and the direction as well as the amount of the transferred momentum $\boldsymbol{q}$. As shown in a thorough treatment by Ma [99], this behaviour of the resonantly excited fluorescence can be traced back to momentum conservation within the resonant inelastic scattering process by making full use of the coupling of absorption and re-emission via the intermediate state as documented in (4.1). By treating the RIXS process as a transition from the ground state into the intermediate state, consisting of a hole in the core

state $|c\rangle$ with energy E_c, and an excited electron in the Bloch state $|\boldsymbol{k}_e\rangle$ with energy $E(\boldsymbol{k}_e)$, followed by the decay of the intermediate state by transition of a valence electron from the Bloch state $|\boldsymbol{k}_h\rangle$ and energy $E(\boldsymbol{k}_h)$ to the core hole, one ends up with

$$\mathrm{d}^2\sigma/\mathrm{d}\Omega\,\mathrm{d}\omega_2 = \sum_{\boldsymbol{k}_e,\boldsymbol{k}_h} |M_{\boldsymbol{k}_c,\boldsymbol{k}_h} M_{\boldsymbol{k}_c,\boldsymbol{k}_e}|^2 \delta(E(\boldsymbol{k}_e) - E_c - \hbar\omega_1)\delta_{\boldsymbol{g},(\boldsymbol{K}_1-\boldsymbol{K}_2+\boldsymbol{k}_h-\boldsymbol{k}_e)} \times \delta(E(\boldsymbol{k}_h) - E_c - \hbar\omega_2) \tag{4.3}$$

where the core state was represented in a tight-binding ansatz ($\boldsymbol{R}$ = lattice transition vector, ϕ_c atomic wavefunction),

$$|c\rangle = \sum_{\boldsymbol{R}} \exp(\mathrm{i}\boldsymbol{k}_c \cdot \boldsymbol{R})\phi_c(\boldsymbol{r} - \boldsymbol{R}) \tag{4.4}$$

$M_{\boldsymbol{k}_c,\boldsymbol{k}_h}$ denotes the matrix element

$$M_{\boldsymbol{k}_c,\boldsymbol{k}_h} = \langle\phi_c|\boldsymbol{e}_2^* \cdot \boldsymbol{p}\exp(-\mathrm{i}\boldsymbol{K}_2 \cdot \boldsymbol{r})|\boldsymbol{k}_h\rangle \tag{4.5}$$

and $M_{\boldsymbol{k}_c,\boldsymbol{k}_e}$ the matrix element

$$M_{\boldsymbol{k}_c,\boldsymbol{k}_e} = \langle k_e|\boldsymbol{e}_1 \cdot \boldsymbol{p}\exp(\mathrm{i}\boldsymbol{K}_1 \cdot \boldsymbol{r})|\phi_c\rangle. \tag{4.6}$$

Equation (4.3) reflects both the energy conservation connected with the absorption and the re-emission process and the crystal momentum conservation, which governs the whole resonant inelastic scattering processes, so that the momentum transfer $\boldsymbol{q} = \boldsymbol{K}_1 - \boldsymbol{K}_2$ must be equal to the vector difference $\boldsymbol{k}_e - \boldsymbol{k}_h$ between the Bloch vectors of the excited electron and that of the hole left behind, modulo a reciprocal lattice vector $\boldsymbol{g}$. This property makes RIXS Bloch-$\boldsymbol{k}$-vector selective, as demonstrated in figure 20 related to a band structure calculation of NiAl [98]: the incident photon energy $\hbar\omega_1$ defines that part of the unoccupied band structure which can be occupied by the excited electron. The energy width of that part is determined by the lifetime broadening of the core level. Bloch-$\boldsymbol{k}$-space regions with high DOS are preferably involved in the excitation, in figure 20 the R-point. Then a distinct Bloch-$\boldsymbol{k}$-space region, separated by the vector of the momentum transfer $\boldsymbol{q}$ from the former $\boldsymbol{k}$-space region, is preferably contributing to the re-emission from the occupied valence band. A series of constant-$\boldsymbol{q}$ RIXS spectra of NiAl measured for incident photon energies by E above the NiK-edge and calculated for the Ni site are shown, as an example, in figure 21. It has been shown by several authors [100] how band structure information can be drawn from Bloch-$\boldsymbol{k}$-selective RIXS spectra.

In contrast to angle-resolved photoelectron spectroscopy (ARPES), which exhibits a similar Bloch-$\boldsymbol{k}$-vector selectivity, RIXS is both element specific, offering thus a higher degree of selectivity for compounds, and symmetry selective, since the matrix elements (4.5) and (4.6) prefer certain symmetries of the conduction and of the valence band states due to the strong preference of dipole transitions.

However, it is a shortcoming of RIXS, when compared with ARPES, that relaxation processes in the intermediate state can partly abolish the Bloch-$\boldsymbol{k}$-vector selectivity, where the relaxation can either be due to Coulomb interaction between the core hole and the excited electron as discussed by van Veenendaal and Carra [101], or, as shown in [100], by electron–phonon or electron–electron scattering. The electron–phonon contribution to relaxation is mainly determined by the ratio of the core hole decay rate R_c and the electron–phonon scattering rate R_{ph}, resulting in a $\boldsymbol{k}$-selective fraction f [100]

$$f = R_c/(R_c + R_{ph}). \tag{4.7}$$

If one compares soft with hard x-ray RIXS, the latter has a much higher f according to (4.7) since $R_c \gg R_{ph}$, but the large R_c of the core hole excited by hard x-rays causes a rather large broadening of the spectra as indicated in figure 20. On the other hand, hard x-ray RIXS probes the real bulk rather than the part of the sample near the surface, and offers the momentum transfer $\boldsymbol{q}$ as an additional degree of freedom in the hand of the experimentalist.

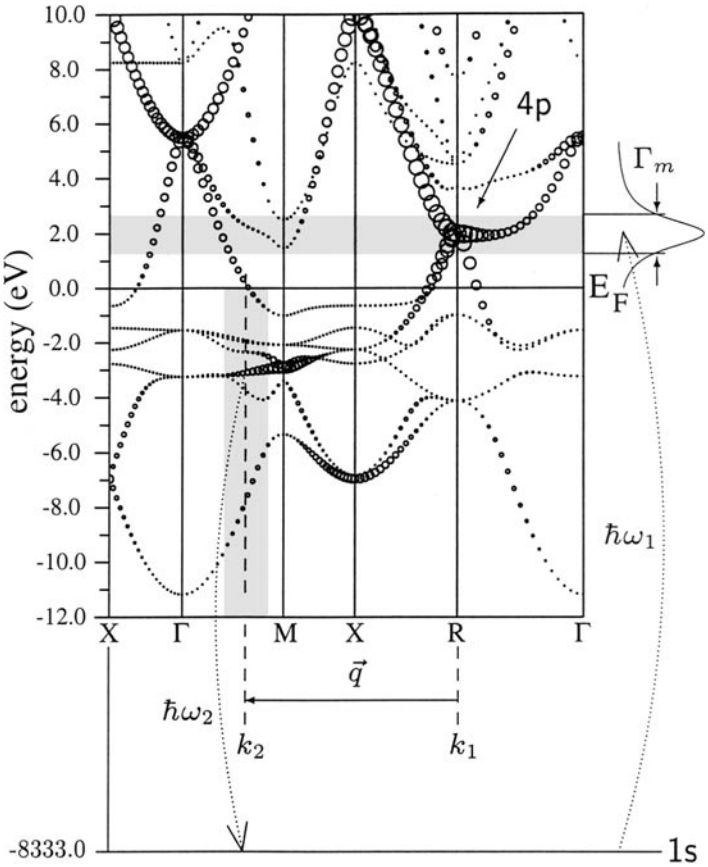

Figure 20. Bloch-$\boldsymbol{k}$-selective RIXS demonstrated at the Ni-site projected LAPW calculated band structure of NiAl as described in the text. The diameter of the open circles is proportional to the partial p-state density at the Ni site.

4.4. Spin selective RIXS, internal spin reference

It was first shown by Hämäläinen *et al* [90] that RIXS can be used to investigate the DOS of unoccupied states spin selectively. This effect is demonstrated schematically in figure 22 for the case of the resonantly excited Eu L$\beta_{2,15}$ ($2p_{3/2}4d$) emission in EuO. The Eu L$\beta_{2,15}$ emission consists of a main line and a satellite, 23 eV lower in energy than the main line. One knows from atomic multiplet calculations and measurements of the circular dichroism of the Eu L$\beta_{2,15}$ emission [102] that, due to the exchange interaction between 4f and 4d states, those atomic multiplets of the $4f^74d^9$ final-state configuration, which correspond to the main line emission, have a spin orientation mostly parallel to the spin of the 4f electrons (majority spin, spin up), whereas the satellite can be traced back to multiplets of the $4f^74d^9$ final-state configuration with nearly pure minority spin (spin down), as shown in figure 22 in a rather simple atomic picture. Let the incident photon excite an electron from the Eu $2p_{3/2}$ core level into the 5d conduction band, where the spin of this electron might be antiparallel (spin down) to the aligned 4f spins of Eu, which acts as an internal (atomic) spin reference. Since we are claiming spin conservation for the whole resonant scattering process, the core hole can be filled up only by an electron with spin down, so that the emission is into the main line.

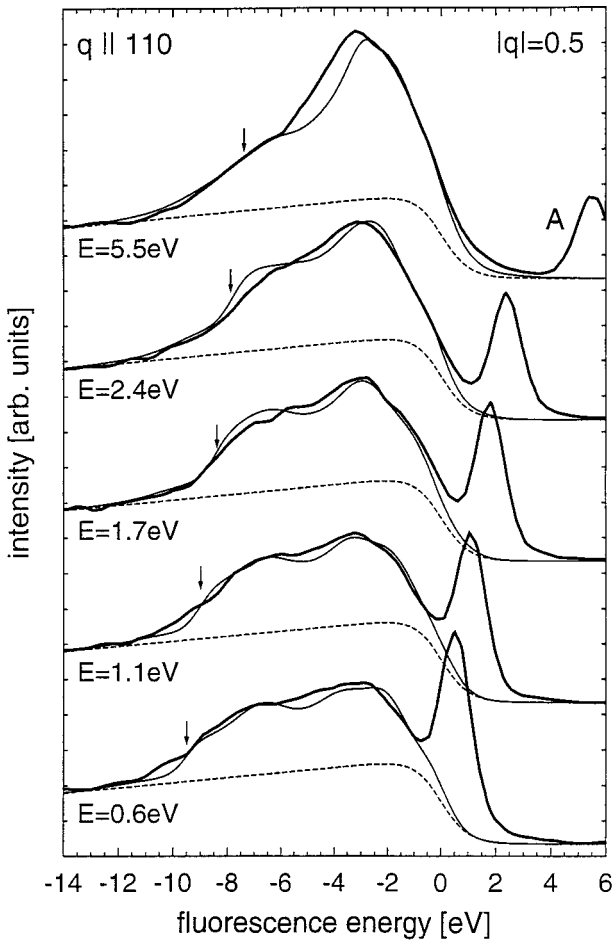

Figure 21. Constant-q RIXS spectra of NiAl with $q \parallel [110]$. Both the incident photon energy E and the energy of the valence band fluorescence have their zero at the Ni 1s binding energy. Bold full curve, experiment; thin full curve, LAPW calculation; dashed curve, estimated shakeup satellite.

If, on the other hand, an electron from the $2p_{3/2}$ core level is excited into a spin-up state of the unoccupied 5d band, the core hole must be filled up by an electron with spin up, so that the emission is into the satellite. Therefore, by setting the analyser energy on the main line and by scanning the incident energy over the Eu L_{III} edge one probes the 5d spin down DOS at the Eu atom, whereas, with the analyser energy on the satellite, the spin-up 5d DOS is investigated. Of course, this simplified description neglects the energy dependence of the contributing dipole matrix elements (4.5) and (4.6). Figure 23 shows the result of such a measurement on EuO at room temperature, this means in the paramagnetic phase [103]. It should be stressed that, contrary to measurements utilizing the magnetic circular dichroism (MCD) [104], where magnetically ordered samples are necessary, this spin selective probing of the unoccupied local DOS does not need a spin ordered state, since the spin orientation of the state under investigation is related to an internal *atomic* spin reference, here the aligned 4f spins of the Eu ion. According to the application of the so-called s(d)–f model [105] (coupling of the s(d)-type conduction electrons with the localized magnetic moments of the

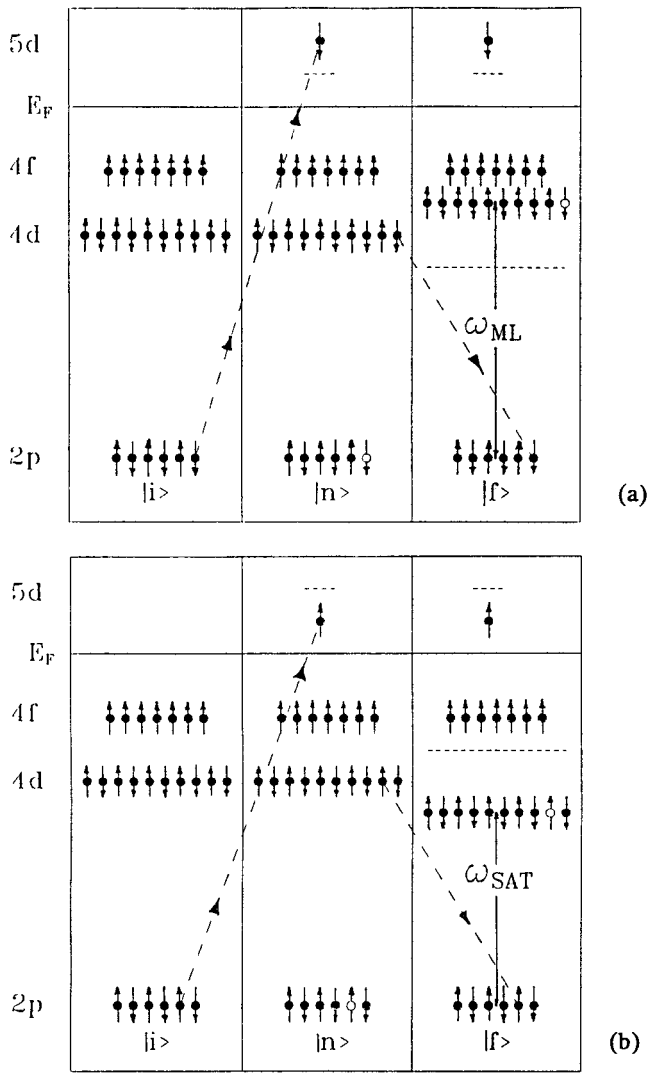

Figure 22. (a) A simple atomic picture of the resonantly excited main-line (ML) Eu L$\beta_{2,15}$ emission of EuO, demonstrating the effect of the internal spin reference offered by the spin polarization of the 4f-level. (b) The same as (a) but for satellite (SAT) Eu L$\beta_{2,15}$ emission.

f-type electrons by exchange interaction) to the ferromagnetic semiconductor EuO by Nolting *et al* [106], the measured shift ΔE of 0.7 eV between the spin-down and spin-up edges can be directly attributed to the coupling constant g of the s(d)–f model via

$$\Delta E = gS, \tag{4.8}$$

where S is the total spin of the 4f electrons ($S = 7/2$), thus ending up with $g = 0.2$ eV, in good agreement with the results of the measured so-called red-shift of the excitation edge of the optical $4f^7 5d^0 \rightarrow 4f^6 5d^1$ transition [107].

Further applications of this technique to MnP [108], and a corresponding theoretical analysis of spin selective RIXS spectra of MnO and MnF_2 [109] should be mentioned,

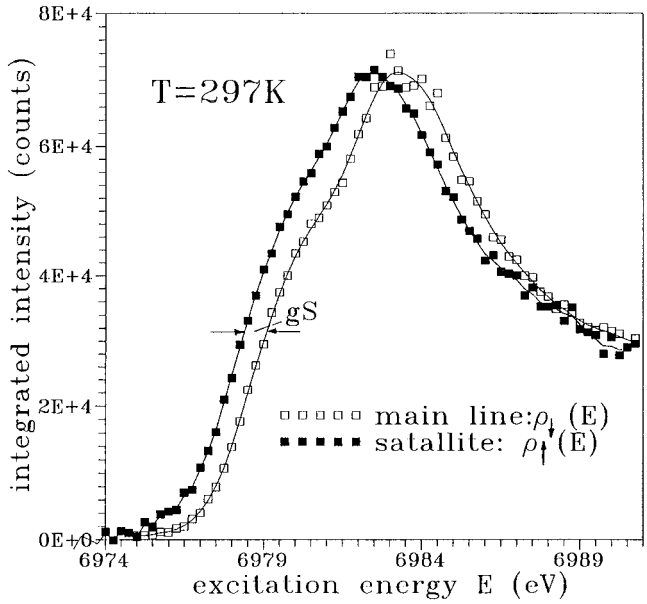

Figure 23. Open squares, integrated intensity of the EuO mean line Eu L$\beta_{2,15}$ emission as a function of the excitation energy for the unoccupied 5d spin-down DOS (open squares) and for the unoccupied 5d spin-up DOS (full squares).

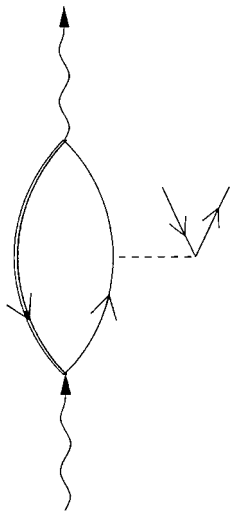

Figure 24. Shakeup processes in the intermediate state. The double line is the propagator of the core hole, the single line is the particle propagator, the dashed line means Coulomb interaction with the surrounding medium producing a particle–hole pair excitation.

especially since in [108] the comparison between the spin selective RIXS spectra with the MCD spectra, measured both at the Mn K-edge, allows the determination of the energy dependence of the Fano factor [104].

4.5. Shakeup processes in the intermediate state

It has been stressed by Platzman and Isaacs [110] that shakeup processes in the intermediate state, as sketched by the diagram of figure 24, open a new window for the investigation of electronic excitations. Abbamonte *et al* [111] have treated such a shakeup processes in third-order perturbation theory interpreting RIXS spectra of La_2CuO_4 taken with the incident energy tuned near the Cu K absorption edge. Applied to this system, the diagram of figure 24 stands for the following processes. The incident photon creates a virtual $\underline{1s}4p$ pair on a copper site ($\underline{1s}$ means a 1s core hole), which is very localized. This pair is bound as an exciton by the Coulomb interaction, takes up the momentum of the incident photon and scatters off the valence electron system producing an excitation, for example a particle–hole excitation. When the exciton recombines, the emitted photon reflects the energy and momentum imparted to the system. Therefore, the scattering amplitude has to be calculated in third-order perturbation theory (second order in $\boldsymbol{p}\cdot\boldsymbol{A}$ and first order in the Coulomb interaction) as follows:

$$S_{if} = \sum_{\underline{1s}4p} M_{em} M_{Coul} M_{abs} / [(E_2 - E_{\underline{1s}4p} + i\Gamma_K/2)(E_1 - E_{\underline{1s}4p} + i\Gamma_K/2)] \tag{4.9}$$

where E_1 and E_2 are the energies of the incident and the scattered photons, respectively, the sum is over all states of the 1s hole and 4p electron, $E_{\underline{1s}4p}$ is their energy and is Γ_K^{-1} the lifetime of the 1s hole. M_{em} is the matrix element of the re-emission process, M_{abs} the matrix element of the absorption process and M_{Coul} the matrix element, which governs the Coulomb interaction induced excitation by the intermediate state and which reads for the case exemplified

$$M_{Coul} = \sum_{\boldsymbol{g}} (4\pi e^2/|\boldsymbol{q}+\boldsymbol{g}|^2) F_{\underline{1s}4p}(\boldsymbol{q}+\boldsymbol{g}, \boldsymbol{e}_0) \langle f|\rho_{v\cdot\boldsymbol{q}+\boldsymbol{g}}|i\rangle \tag{4.10}$$

where $F_{\underline{1s}4p}$ ($(\boldsymbol{k})$ is the x-ray static structure factor of the $\underline{1s}4p$ exciton, $\langle f|$ and $\langle i|$ denote the final and the initial states, and $\rho_{v\cdot\boldsymbol{q}+\boldsymbol{g}}$ is the valence part of the many body density operator. Equation (4.9) along with (4.10) indicates that there are two signatures, which give evidence for a shakeup process as described above:

(1) the double resonance denominator in (4.9) gives rise to deviations from the simple linear relationship between incident energy and scattered photon energy in a RIXS process for incident energies smaller than the threshold, as depicted in subsection 4.1 under the designation Raman shift;
(2) M_{Coul} of (4.10) means that the intensity of the RIXS spectra brought about by processes described by (4.9) must have a characteristic dependency on $\boldsymbol{q}$.

As an example, we plot in figure 25 a series of RIXS spectra of CuO for different incident photon energies tuned near the Cu K-edge as a function of energy loss. γ is the angle between the surface normal of the sample and the incident beam and determines the angles between the polarization vector of the incident beam and the two types of CuO planes in the monoclinic CuO crystal and, therefore, the ratio of $1s4p_\sigma$ to $1s4p_\pi$ excitons in (4.9). Referring to the cluster calculations of Eskes *et al* [112] we attribute the peak structure, marked by a bar, between the (quasi)elastically scattered line and the Cu-valence band emission to a satellite due to a shakeup transition from the b_{1g} ground state to a high-energy a_{1g} excited state. It is clearly visible in figure 25 that the peak position of this structure is incident energy dependent and does not exhibit the simple Raman-shift behaviour described in subsection 4.1, which should give a non-varying position if plotted as a function of energy loss. We ascribe this behaviour to the double resonance denominator of (4.9), so that a treatment in third-order perturbation theory seems to be advisable. Moreover, looking at the satellite for a given incident energy but measured with different amounts (and directions) of momentum transfer $\boldsymbol{q}$, as shown in

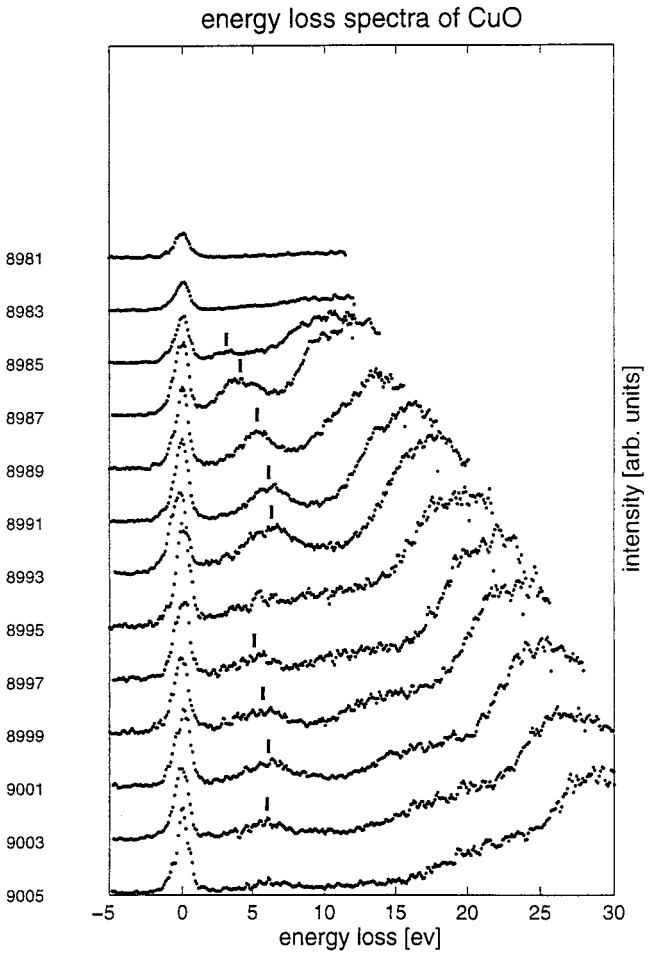

Figure 25. Constant-q resonant energy loss spectrum of CuO for different incident photon energies as indicated, tuned near the Cu K-edge. The bars mark the peak position of the shakeup satellite; $\gamma = 54^\circ$.

figure 26, one recognizes a big difference in intensity if we normalize to the intensity of the valence band emission. This difference can be traced back to the $\boldsymbol{q}$ dependence of the Coulomb matrix element (4.10), again a hint that it is Coulomb interaction induced excitation by the intermediate state, which has to be treated in third-order perturbation theory.

If one accepts this interpretation of structures in the RIXS spectra, resonant inelastic x-ray scattering opens a unique possibility to investigate element-specific and resonantly-enhanced electronic excitations and especially their dispersion, since, as stated above, the full momentum $\boldsymbol{q} = \boldsymbol{K}_1 - \boldsymbol{K}_2$ is imparted to the shakeup excitation, if other relaxation processes such as phonon emission are neglected. Thus Tsutsui *et al* [113] have proposed the utilization of this momentum dependence of shakeup satellites of RIXS spectra to probe the charge gap in a Mott insulator (insulating cuprates) through the creation of a hole in the occupied Zhang–Rice band (ZRB) [114], thereby promoting an electron across the gap to the unoccupied upper Hubbard band (UHB) with a finite momentum transferred to the system tunable in size and direction. These experiments have been performed by Hasan *et al* [115] and have shown,

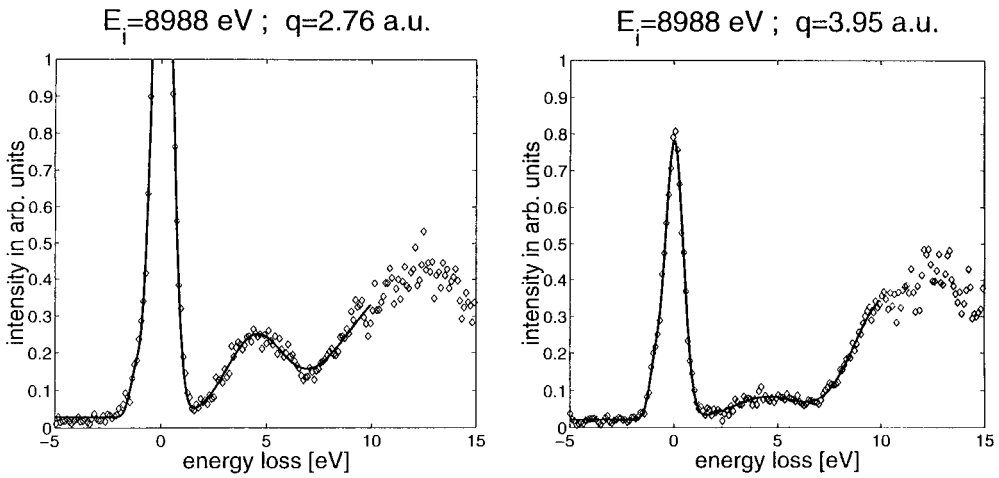

Figure 26. Dependence of the CuO shakeup peak intensity on the value of the indicated momentum transfer q, measured with constant incident photon energy. The spectra are normalized to the intensity of the CuO valence band emission.

in good agreement with the predictions of [114], a partial doublet nature of the excitations and a strongly anisotropic dispersion. The results of these experiments could help to fill the gaps of knowledge about the momentum-resolved electronic structure of the UHB, which is of importance for understanding the physics of n-type superconductors, since the doped electrons occupy the UHB.

RIXS experiments, performed somewhat earlier than those mentioned above, and which were also devoted to the investigation of spectral features due to excitations connected with charge transfer in NiO (the pioneering experiment of Kao *et al* [116]) and Nd_2CuO_4 [117, 118] have been interpreted in another way even if the physics behind them seems not to be so different to the experiments interpreted in third-order perturbation theory. The authors did not see the need to treat the scattering process in third-order perturbation theory, but remained in second order, thus having only a single resonance denominator and a simple linear Raman shift. Their interpretation of charge transfer features in the RIXS spectra is based on the Anderson impurity model [119], where, for the case of the cuprates, the Cu $3d^9$ configuration hybridizes with $3d^{10}\underline{L}$, where $\underline{L}$ represents an O 2p ligand hole, so that the ground state is the bonding state with about 60% of the $3d^9$ configuration whereas the antibonding state, which is Δ apart in energy from the ground state, is mainly $3d^{10}\underline{L}$ with a continuous band between them. If in the intermediate state a Cu 1s electron is excited to the Cu $4p_{\pi/\sigma}$ conduction band, the core hole potential reverses the balance between the $3d^9$ and the $3d^{10}\underline{L}$ configurations, so that the bonding state with predominantly $\underline{1s}3d^{10}\underline{L}4p$ is lower in energy than the antibonding state $\underline{1s}3d^9 4p$. If either of these intermediate states decays into the antibonding excited states an energy loss of Δ would result. This energy loss is found in the experiment. Since both the energy shift of the RIXS spectra with the incident energy is simple Raman like and no $\boldsymbol{q}$-dependence of the intensity of the RIXS spectra could be found [118] in the above-mentioned cases, the interpretation of the spectra within the limits of the second-order perturbation theory seems to be conclusive. It remains a matter of debate whether different materials under investigation need different theoretical treatments or not.

Acknowledgments

The author thanks K Hämäläinen and A Kaprolat for helpful discussions. Unpublished results were provided by Chr Wittkop, G Döring and A Kaprolat. This work was supported by the German Federal Ministry of Education and Research under contract Nos 05 ST 8 HRA and 05 SC8 PEA4.

References

[1] Nozieres P and Pines D 1959 *Phys. Rev.* **113** 1254
[2] Priftis G 1970 *Phys. Rev.* B **2** 54
[3] Alexandropoulos N G 1971 *J. Phys. Soc. Japan* **31** 1790
[4] Eisenberger P, Platzman P M and Pandy K C 1973 *Phys. Rev. Lett.* **31** 311
[5] Schülke W, Berg U and Brümmer O 1969 *Phys. Status Solidi* **35** 227
[6] Platzman P M and Eisenberger P 1974 *Phys. Rev. Lett.* **33** 152
[7] Platzman P M and Eisenberger P 1974 *Solid State Commun.* **14** 1
[8] Schülke W and Lautner W 1974 *Phys. Status Solidi* b **66** 211
[9] Eisenberger P, Platzman P M and Schmidt P 1975 *Phys. Rev. Lett.* **34** 18
[10] Eisenberger P and Platzman P M 1976 *Phys. Rev. Lett.* B **13** 934
[11] Schülke W, Nagasawa H, Mourikis S and Lanzki P 1986 *Phys. Rev.* B **33** 6744
[12] Schülke W, Nagasawa H and Mourikis S 1984 *Phys. Rev. Lett.* **52** 2065
[13] Eisenberger P, Platzman P M and Winick H 1976 *Phys. Rev. Lett.* **36** 623
[14] Eisenberger P, Platzman P M and Winick H 1976 *Phys. Rev.* B **13** 2377
[15] Schülke W 1991 Inelastic scattering by electronic excitations *Handbook on Synchrotron Radiation* vol 3, ed G Brown and D E Moncton (Amsterdam: Elsevier) pp 565–637
[16] Lindhard J 1954 Matematisk-Fysiske Meddelel **28** 8
[17] Schülke W, Schulte-Schrepping H and Schmitz J R 1993 *Phys. Rev.* B **47** 12 426
[18] Mahan G D 1981 *Many Particle Physics* (New York: Plenum) pp 422–37
[19] Hills J P, Kao C-C, Caliebe W A C, Gibbs D and Hastings J B 1996 *Phys. Rev. Lett.* **77** 3665
[20] Raether H 1980 *Excitation of Plasmons and Interband Transitions by Electrons* (Berlin: Springer)
[21] Schülke W, Nagasawa H, Mourikis S and Kaprolat A 1989 *Phys. Rev.* B **40** 12 215
[22] Sternemann C, Kaprolat A and Schülke W 1998 *Phys. Rev.* B **57** 622
[23] Qoung A A and Eguiluz A G 1993 *Phys. Rev. Lett.* **70** 3955
[24] Ehrenreich H and Cohen M H 1959 *Phys. Rev.* **115** 786
[25] Ashcroft N W and Mermin N D 1976 *Solid State Physics* (New York: Holt, Rinehard and Winston) p 99
[26] Foo E Ni and Hopfield J J 1968 *Phys. Rev.* **173** 635
[27] Sturm K and Oliviera L E 1984 *Phys. Rev.* B **30** 4351
[28] Burkel E 1991 *Inelastic Scattering of X-rays with Very High Energy Resolution* (Berlin: Springer) pp 85–9
[29] Schülke W, Bonse U, Nagasawa H, Mourikis S and Kaprolat W 1987 *Phys. Rev. Lett.* **59** 1361
[30] Maddocks N E, Godby R W and Needs R J 1994 *Phys. Rev.* B **49** 8502
[31] Taut M and Hanke W 1976 *Phys. Status Solidi* b **77** 543
[32] Platzman P M, Isaacs E D, Williams H, Zschack P and Ice G E 1992 *Phys. Rev.* B **46** 12 943
[33] Mukhopadhyay G, Kalia R K and Singwi K S 1975 *Phys. Rev. Lett.* **34** 950
[34] Ng T K and Dabrowski B 1986 *Phys. Rev.* B **33** 5358
[35] Ojala E 1983 *Phys. Status Solidi* b **119** 269
[36] Maddocks N E, Godby R W and Needs R J 1994 *Europhys. Lett.* **27** 681
[37] Fleszar A, Quong A A and Eguiluz A G 1995 *Phys. Rev. Lett.* **74** 590
[38] Schülke W, Schmitz J R, Schulte-Schrepping H and Kaprolat A 1995 *Phys. Rev.* B **52** 11 721
[39] Caliebe W A, Soininen J A, Shirley E L, Kao C-C and Hämäläinen K 2000 *Phys. Rev. Lett.* **84** 3907
[40] Schülke W, Bonse U, Nagasawa H, Kaprolat A and Berthold A 1988 *Phys. Rev.* B **38** 2112
[41] Schülke W, Berthold A, Kaprolat A and Güntherodt H-J 1988 *Phys. Rev. Lett.* **60** 2217
[42] Posternak M, Baldereshi A, Freeman A J, Wimmer E and Weinert M 1983 *Phys. Rev. Lett.* **50** 761
[43] Holzwarth N A W, Louie S G and Rabii S 1984 *Phys. Rev.* B **30** 2219
[44] Schülke W, Berthold A, Schulte-Schrepping H, Gabriel K-J, Thommes-Geiser V and Güntherodt H-J 1991 *Solid State Commun.* **79** 661
[45] Mizuno Y and Ohmura Y 1967 *J. Phys. Soc. Japan* **22** 445
[46] Nagasawa H, Mourikis S and Schülke W 1989 *J. Phys. Soc. Japan* **58** 710
[47] Tohji K and Udagawa Y 1987 *Phys. Rev.* B **36** 9410

[48] Schülke W, Gabriel K-J, Berthold A and Schulte-Schrepping H 1991 *Solid State Commun.* **79** 657
[49] Holzwarth N A W, Louie S G and Rabii S 1983 *Phys. Rev.* B **28** 1013
[50] Bowron D T, Krisch M H, Barnes A C, Finney J L, Kaprolat A and Lorenzen M 2000 *Phys. Rev.* B
[51] Schell N, Simmons R O, Kaprolat A, Schülke W and Burkel E 1995 *Phys. Rev. Lett.* **74** 2535
[52] Krisch M H, Sette F, Masciovecchio C and Verbeni R 1997 *Phys. Rev. Lett.* **78** 2843
[53] Nagasawa H, Mourikis S and Schülke W 1997 *J. Phys. Soc. Japan* **66** 3139
[54] Mahan G D 1967 *Phys. Rev.* **163** 612
Nozieres P and DeDominicis 1969 *Phys. Rev.* **178** 1097
[55] Girvin S M and Hopfield J J 1976 *Phys. Rev. Lett.* **37** 1091
[56] Hedin L 1965 *Phys. Rev.* **139** A796
[57] Schrieffer J R 1964 *Theory of Superconductivity* (New York: Benjamin)
[58] Green F, Neilson D and Szymanski J 1985 *Phys. Rev.* B **31** 2796
Green F, Neilson D and Szymanski J 1987 *Phys. Rev.* B **5** 124
[59] Lundqvist B I 1967 *Phys. Kondens. Materie* **6** 193
[60] Baym G and Kadanoff L 1961 *Phys. Rev.* **124** 287
[61] Sternemann C, Hämäläinen K, Kaprolat A, Soininen A, Döring G, Kao C-C, Manninen S and Schülke W 2000 *Phys. Rev.* B **62** 7686
[62] Beeferman L W and Ehrenreich H 1970 *Phys. Rev.* B **2** 364
[63] Holm B and Aryasetiawan 1997 *Phys. Rev.* B **56** 12 825
[64] Sturm K and Gusarov A 2000 *Phys. Rev.* B **62** 16 474
[65] Geldart D J W and Vosko S H 1966 *Can. J. Phys.* **44** 2137
[66] Hubbard J 1958 *Proc. R. Soc.* A **243** 336
[67] Kugler A A 1975 *J. Stat. Phys.* **12** 35
[68] Utsumi K and Ichimaru S 1980 *Phys. Rev.* B **22** 5203
[69] Schülke W, Höppner K and Kaprolat A 1996 *Phys. Rev.* B **54** 17 464
[70] Farid B, Heine V, Engel G E and Robertson I J 1993 *Phys. Rev.* B **48** 11 602
[71] Larson B C, Tischler J Z, Isaacs E D, Zschack P, Fleszar A and Eguiluz A G 1996 *Phys. Rev. Lett.* **77** 1346
[72] Benedict L X and Shirley L E 1999 *Phys. Rev.* B **59** 5441
[73] Wiser N 1963 *Phys. Rev.* **129** 62
[74] Saslow W M and Reiter G F 1973 *Phys. Rev.* B **7** 2995
[75] Schülke W 1981 *Phys. Lett.* A **83** 451
[76] Schülke W 1982 *Solid State Commun.* **43** 863
[77] Schülke W and Kaprolat A 1991 *Phys. Rev. Lett.* **67** 879
[78] v. Laue M 1960 *Röntgenstrahlinterferenzen* (Frankfurt/Main: Akademische Verlagsgesellschaft)
[79] Girlanda R, Parinello M and Torsati E 1976 *Phys. Rev. Lett.* **44** 1386
[80] Oliveira L E and Sturm K 1980 *Phys. Rev.* B **22** 6283
[81] Sturm K and Schülke W 1992 *Phys. Rev.* B **46** 7193
[82] Daling R, von Haeringen W and Farid B 1991 *Phys. Rev.* **44** 2952
[83] Fano U 1961 *Phys. Rev.* **124** 1866
[84] Sturm K, Schülke W and Schmitz J R 1992 *Phys. Rev. Lett.* **68** 228
[85] Höppner K, Kaprolat A and Schülke W 1998 *Eur. Phys. J.* B **5** 53
[86] Bross H and Ehrnsperger M 1995 *Z. Phys.* B **97** 17
[87] Tulkki J and Aberg T 1980 *J. Phys. B: At. Mol. Phys.* **13** 3341
[88] Ma Y, Wassdahl N, Skytt P, Guo J, Nordgren J, Johnson P D, Rubensson J E, Boske T, Eberhardt W and Kevan S 1992 *Phys. Rev. Lett.* **69** 2598
[89] Johnson P D and Ma Y 1994 *Phys. Rev.* B **49** 5024
[90] Hämäläinen K, Kao C-C, Hastings J B, Siddons D P, Berman L E, Stojanoff V and Cramer S P 1992 *Phys. Rev.* B **46** 14 274
[91] Hämäläinen K, Manninen S, Suorti P, Collins S P, Cooper M J and Laundy D 1989 *J. Phys.: Condens. Matter* **1** 1
[92] Hämäläinen K, Manninen S, Collins S P and Cooper M J 1990 *J. Phys.: Condens. Matter* **2** 5619
[93] Hämäläinen K, Siddons D P, Hastings J B and Berman L E 1991 *Phys. Rev. Lett.* **67** 2850
[94] Krisch M, Kao C-C, Sette F, Caliebe W A, Hämäläinen K and Hastings J B 1995 *Phys. Rev. Lett.* **74** 152
[95] Bartolome F, Tonnerre J M, Seve L, Raoux D, Chaboy J, Garcia L M, Krisch M H and Kao C C 1997 *Phys. Rev. Lett.* **79** 3775
[96] Döring G, Enkisch H, Sternemann C and Schülke W 2001 *HASYLAB Annual Report* p 309
[97] Miyano K E, Ederer D L, Callcott T A, O'Brien W L, Jia J J, Zhou L, Dong Q Y, Ma Y and Woicik J C and Mueller D R 1993 *Phys. Rev.* B **48** 1918

[98] Eniksch H, Kaprolat A, Schülke W, Krisch M H and Lorenzen M 1999 *Phys. Rev.* B **60** 8624
[99] Ma Y 1994 *Phys. Rev.* B **49** 5799
[100] See for a review Eisebitt S and Eberhardt W 2000 *J. Electron Spectrosc. Related Phenom.* **110–111** 335
[101] van Veenendaal M and Carra P 1997 *Phys. Rev. Lett.* **78** 2839
[102] Wittkop C, Schülke W and de Groot F M F 2000 *Phys. Rev.* B **61** 7176
[103] Wittkop C 2000 Spinselektive Messung der unbesetzten 5d Zustandsdichte von EuO mit resonanter unelastischer Röntgenstreuung (RIXS) *Thesis* University of Dortmund
[104] Schütz G, Wagner W, Wilhelm W, Kienle P, Zeller R, Frahm R and Materlik G 1987 *Phys. Rev. Lett.* **58** 737
[105] Sinkkonen J 1979 *Phys. Rev.* B **19** 6407
[106] Nolting W, Borstel G and Borgsiel W 1987 *Phys. Rev.* B **35** 7015
Nolting W, Borgsiel W and Borstel G 1987 *Phys. Rev.* B **35** 7025
[107] Schoenes J and Wachter P 1975 *Phys. Rev.* B **9** 3097
[108] de Groot F M F, Pizzini S, Fontaine A, Hämäläinen K, Kao C-C and Hastings J B 1995 *Phys. Rev.* B **51** 1045
[109] Soldatov A V, Ivanchenko T S, Kovtun A P, Dealla Longa S and Bianconi A 1995 *Phys. Rev.* B **52** 11 757
[110] Platzman P M and Isaacs E D 1998 *Phys. Rev.* B **57** 107
[111] Abbamonte P, Burns C A, Isaacs E D, Platzman P M, Miller L L, Cheong S W and Klein M V 1999 *Phys. Rev. Lett.* **83** 860
[112] Eskes H, Tjeng L H and Sawatzky G A 1990 *Phys. Rev.* B **41** 288
[113] Tsutsui K, Tohyama T and Maekawa S 1999 *Phys. Rev. Lett.* **83** 3705
[114] Zhang F C and Rice T M 1988 *Phys. Rev.* B **37** 3759
[115] Hasan M Z, Isaacs E D, Shen Z-X, Miller L L, Tsutsui K, Tohyama T and Maekawa S 2000 *Science* **288** 1811
[116] Kao C-C, Caliebe W A L, Hastings J B and Gillet J-M 1996 *Phys. Rev.* B **54** 16 361
[117] Hill J P, Kao C-C, Caliebe W A L, Matsubara M, Kotani A, Peng J L and Greene R L 1998 *Phys. Rev. Lett.* **80** 4967
[118] Hämäläinen K, Hill J P, Huotari S, Kao C-C, Berman L E, Kotani A, Ide T, Peng J L and Greene R L 2000 *Phys. Rev.* B **61** 1836
[119] Tanaka S, Okada K and Kotani A 1991 *J. Phys. Soc. Japan* **60** 3893
Tanaka S and Kotani A 1993 *J. Phys. Soc. Japan* **62** 464